



LAWRENCE  
LIVERMORE  
NATIONAL  
LABORATORY

UCRL-TR-204870

# **Nuclear Melt Glass Dissolution and Secondary Mineral Precipitation at 40 to 200°C**

*M. Zavarin, S.K. Roberts, B.E. Viani,  
G.A. Pawloski, and T.P. Rose*

**February 2004**

### Disclaimer

This document was prepared as an account of work sponsored by an agency of the United States Government. Neither the United States Government nor the University of California nor any of their employees, makes any warranty, express or implied, or assumes any legal liability or responsibility for the accuracy, completeness, or usefulness of any information, apparatus, product, or process disclosed, or represents that its use would not infringe privately owned rights. Reference herein to any specific commercial product, process, or service by trade name, trademark, manufacturer, or otherwise, does not necessarily constitute or imply its endorsement, recommendation, or favoring by the United States Government or the University of California. The views and opinions of authors expressed herein do not necessarily state or reflect those of the United States Government or the University of California, and shall not be used for advertising or product endorsement purposes.

### Auspices Statement

This work was performed under the auspices of the U.S. Department of Energy by University of California, Lawrence Livermore National Laboratory under Contract W-7405-Eng-48.

This report has been reproduced  
directly from the best available copy.

Available to DOE and DOE contractors from the  
Office of Scientific and Technical Information  
P.O. Box 62, Oak Ridge, TN 37831  
Prices available from (423) 576-8401  
<http://apollo.osti.gov/bridge>

Available to the public from the  
National Technical Information Service  
U.S. Department of Commerce  
5285 Port Royal Rd,  
Springfield, VA 22161  
<http://www.ntis.gov/>

OR

Lawrence Livermore National Laboratory  
Technical Information Department's Digital Library  
<http://www.llnl.gov/library/>

# **Nuclear Melt Glass Dissolution and Secondary Mineral Precipitation at 40 to 200°C**

Mavrik Zavarin<sup>a</sup>, Sarah K. Roberts<sup>a</sup>, Brian Viani<sup>a</sup>,  
Gayle A. Pawloski<sup>a</sup>, and Timothy P. Rose<sup>b</sup>

<sup>a</sup>Geosciences and Environmental Technologies Division,  
<sup>b</sup>Chemical Biology and Nuclear Science,  
Lawrence Livermore National Laboratory  
Livermore, California

Prepared for the Underground Test Area Project  
U. S. Department of Energy  
National Nuclear Security Administration  
Nevada Site Office

Final Report

February 1, 2004





## TABLE OF CONTENTS

<b>1</b>	<b>INTRODUCTION .....</b>	<b>1</b>
<b>2</b>	<b>EXPERIMENTAL PROCEDURE .....</b>	<b>3</b>
	2.1 Nuclear Melt Glass Preparation .....	3
	2.2 Scanning Electron Microscopy and X-ray Diffraction.....	5
<b>3</b>	<b>RESULTS AND DISCUSSION .....</b>	<b>5</b>
	3.1 Solution Conditions .....	6
	3.1.1 <i>SiO<sub>2</sub>(aq) in Solution</i> .....	7
	3.1.2 <i>Saturation State of Solutions</i> .....	10
	3.1.3 <i>Redox State of Solutions</i> .....	15
	3.2 Predicted Glass Dissolution Rates.....	17
	3.3 Identification of Secondary Minerals .....	19
	3.3.1 <i>Scanning Electron Microscopy</i> .....	19
	3.3.2 <i>X-Ray Diffraction</i> .....	25
<b>4</b>	<b>SUMMARY .....</b>	<b>29</b>
<b>5</b>	<b>ACKNOWLEDGEMENTS .....</b>	<b>30</b>
<b>6</b>	<b>REFERENCES.....</b>	<b>30</b>
	<b>APPENDIX. SEM Photomicrographs of Unreacted Nuclear Melt Glass</b> <b>(Sample JMK-3) and Reacted Melt Glass (80°C, 120°C, 160°C and 200°C).....</b>	<b>32</b>

## LIST OF FIGURES

Figure 1. Glass dissolution rate with time and steady-state pH resulting from variation in the identity and rates of precipitation of secondary minerals. Simulation details reported in Pawloski et al. (2001); 0.1 m/yr Darcy flux simulation results shown.....	2
Figure 2. Si concentration as a function of temperature from batch glass reaction experiments compared to the calculated solubility of amorphous SiO <sub>2</sub> , α-cristobalite, and β-cristobalite based on solution conditions described in Tables 3 and 4. ....	8
Figure 3. Predicted buildup of Si in solution as a function of time for batch glass reaction experiments from 40 to 200°C (ignoring secondary mineral precipitation): The CHESHIRE model of Pawloski et al. (2001) (thin lines), the modified CHESHIRE model of Zavarin et al. (2004) (thick lines), and measured data (circles).....	10
Figure 4. Eh and pH data (at 25°C) from reacted glasses on an Eh – pH diagram of Fe (25°C). Low T samples include 40, 80, and 120°C solutions; high T samples include 160 and 200°C solutions. ....	16
Figure 5. Eh and pH data (at 25°C) from reacted glasses and CHESHIRE model condition on an Eh – pH diagram of Pu (25°C). Low T samples include 40, 80, and 120°C solutions; high T samples include 160 and 200°C solutions. HCO <sub>3</sub> <sup>-</sup> activity set to 10 <sup>-2.6</sup> (predicted HCO <sub>3</sub> <sup>-</sup> activity at pH ~8). ....	16
Figure 6. Predicted glass dissolution as a function of time for solution experiments from 40 to 200°C. Thin lines represent prediction based on the CHESHIRE model (Pawloski et al., 2001). Thick lines represent prediction based on the modified CHESHIRE model (Zavarin et al., 2004). ....	18
Figure 7. SEM photomicrographs of unreacted nuclear melt glass (sample JMK-3). ....	19
Figure 8. SEM photomicrographs of nuclear melt glass reacted at 80°C. ....	20
Figure 9. SEM photomicrographs of nuclear melt glass reacted at 120°C. ....	21
Figure 10. SEM photomicrographs of nuclear melt glass reacted at 160°C.....	22
Figure 11. SEM photomicrographs of nuclear melt glass reacted at 200°C.....	24
Figure 12. XRD spectra of obsidian and laboratory-grade silica glasses. From Palmer et al. (1988). A stacked plot of relative intensities is presented.....	26
Figure 13. XRD spectra of unreacted (JMK-3) and 40, 80, 120, 160, and 200°C reacted nuclear melt glasses. A stacked plot of relative intensities is presented.....	27

Figure 14. Analysis of XRD data of unreacted and 200°C reacted nuclear melt glasses. Spectra were smoothed and background subtracted prior to peak fitting analysis. ....	28
Figure A1. SEM results for the unreacted nuclear melt glass (sample JMK-3). ....	32
Figure A2. SEM results for the 80°C reacted nuclear melt glass. ....	33
Figure A3. SEM results for the 120°C reacted nuclear melt glass. ....	34
Figure A4. SEM results for the 160°C reacted nuclear melt glass. ....	36
Figure A5. SEM results for the 200°C reacted nuclear melt glass. ....	37

## LIST OF TABLES

Table 1. Mass percent oxide composition of JMK-3 melt glass (average based on ~10 microprobe analyses).....	4
Table 2. Gamma spectroscopy results for JMK-3 melt glass.....	4
Table 3. Elemental composition of post reaction solutions.....	6
Table 4. Reaction time, Eh and pH of post reaction solutions. ....	7
Table 5. Minerals observed in devitrified tuffs of Pahute Mesa and their state of saturation in glass dissolution experiments.....	14

## 1 INTRODUCTION

Most long-lived radionuclides associated with an underground nuclear test are initially incorporated into melt glass and become part of the hydrologic source term (HST) only upon their release via glass dissolution (Pawloski et al., 2001). As the melt glass dissolves, secondary minerals precipitate. The types of secondary minerals that precipitate influence the water chemistry in and around the melt glass. The secondary minerals also provide a sorption sink to the released radionuclides. The changing water chemistry affects the rate of glass dissolution; it also affects the sorption behavior of the released radionuclides. This complex nature of glass dissolution and its important role in defining the HST requires a thorough understanding of glass dissolution and secondary mineral precipitation. The identity of secondary minerals formed at temperatures from 40 to 200°C are evaluated in this report to assist in that understanding.

Silicate glasses (such as nuclear melt glass) are known to react with water to form hydrous secondary minerals such as clays and zeolites. The type of secondary mineral that forms depends on the composition of the silicate glass, the temperature, pH, and groundwater composition. The secondary minerals form as a layer on the glass surface. This layer may armor the glass and slow down dissolution rates. However, it is generally not impermeable, and water can diffuse to the underlying melt glass and glass dissolution continues. HST modeling of the CHESHIRE test (Pawloski et al., 2001) has shown that the rates of glass dissolution are very sensitive to the types of secondary minerals that form. Figure 1 illustrates the role that secondary minerals play in the evolution of the groundwater chemistry of the melt glass zone. The data in this figure were taken from Figure 6.21 of Pawloski et al. (2001) which summarized the glass dissolution rate and pH that resulted from a number of flow-through simulations. In general, the results suggest that when clay precipitation dominates, the pH tends to rise. This rise in pH affects both the sorption behavior of radionuclides and the overall rate of glass dissolution. When secondary minerals are assumed to precipitate very slowly, glass dissolution is controlled by the aqueous Si concentration (described as affinity-limited precipitation in Figure 1). This slows the rate of glass dissolution and the pH does not change drastically. When a number of framework silicates (including zeolites) and clays are allowed to precipitate, the pH and the glass dissolution rate remain relatively constant. Based on the data in Figure 1, the rate of glass dissolution at 50 years can vary by more than three orders of magnitude depending on how secondary mineral precipitation is treated in the model.

The type of secondary mineral precipitates that forms as a function of temperature and solution conditions is not constrained sufficiently by our thermodynamic model. Thus, the choice of secondary minerals allowed to precipitate in the glass dissolution model must be constrained based on empirical evidence. For example, zeolites typically form over a temperature range of 100 to 250°C. At lower temperatures, a variety of clays are more likely to form. At higher temperatures, feldspars and other aluminosilicates are likely to form. The range of conditions at which a particular mineral is likely to form is approximate and dependent on the particular solution conditions and glass composition. Because there are so many variables and dependencies in the glass dissolution model,

experimental evidence is necessary to determine the dominant secondary mineral precipitates for the specific conditions of interest.

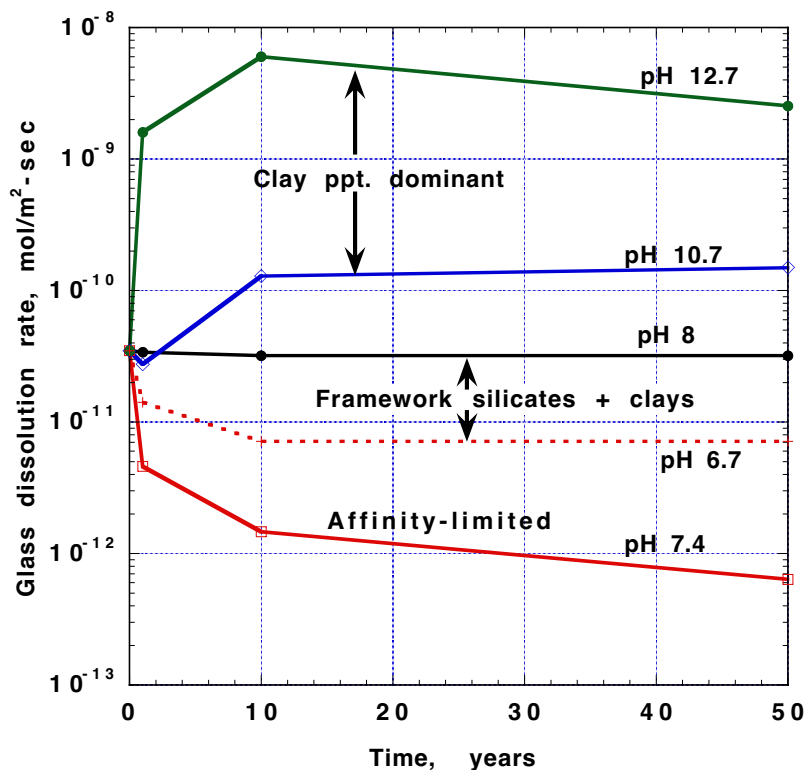


**Figure 1. Glass dissolution rate with time and steady-state pH resulting from variation in the identity and rates of precipitation of secondary minerals. Simulation details reported in Pawloski et al. (2001); 0.1 m/yr Darcy flux simulation results shown.**

To identify the types and compositions of likely secondary minerals, we reacted nuclear melt glass at 5 temperatures (40 to 200°C) in 0.005 mol/L NaHCO<sub>3</sub> waters for a period of ~3 months. The initial water chemistry is a simplified version of average Pahute Mesa groundwater which includes 3×10<sup>-3</sup> mol/L Na, 2×10<sup>-3</sup> mol/L HCO<sub>3</sub>, as well as other minor elements (Pawloski et al., 2001). The range in experimental temperatures spans the temperatures likely to be encountered when groundwater re-saturates the nuclear melt glass zone after a nuclear test. The experiment results reported here will be used to constrain the choice of secondary minerals and glass dissolution rates used in future HST simulations.

## 2 EXPERIMENTAL PROCEDURE

The nuclear melt glass sample (designated as JMK-3) used in the experiments is from an undisclosed underground test that was detonated below the water table on Pahute Mesa, NTS. The sample was collected, characterized, and prepared for dissolution experiments. The sample consists of highly vesicular, colorless to gray-banded glass, similar in appearance to pumice.

The procedure of the reaction tests was as follows:

1. JMK-3 glass was crushed, washed and sieved to a 25-53  $\mu\text{m}$  size fraction.
2. Approximately one gram of glass was loaded into a Teflon or titanium lined pressure vessel with 10 to 20 mL of 0.005 mol/L  $\text{NaHCO}_3$  solution (pH  $\sim$ 8.5).
3. Vessels were sealed and placed in separate furnaces at 40, 80, 120, 160, and 200°C (samples were not stirred during experiments). After a period of several months, the furnaces were shut off, and the vessels cooled to room temperature.
4. Filtered solution samples were drawn from the vessels for inductively coupled plasma atomic emission spectrometry (ICP-AES), pH, and Eh measurements.
5. Glass samples were dried at 40°C.
6. A subset of the dried glass was prepared for x-ray diffraction (XRD) and scanning electron microscopy (SEM) analysis.

Details of melt glass preparation and initial characterization are described in the following section.

### 2.1 Nuclear Melt Glass Preparation

The JMK-3 glass was crushed and sieved to obtain particle sizes of 25-53  $\mu\text{m}$ . This particle size range was chosen to maximize the reactive surface area (i.e. maximize the secondary mineral formation) while minimizing the possibility of particle aggregation and flocculation, which might negatively affect rates of glass dissolution. Particles with diameters of  $<25 \mu\text{m}$  were removed by wet-sieving the glass with water followed by acetone. The major element composition of the nuclear melt glass was analyzed on a JEOL 8200 electron microprobe using a 7.5 nA, 15 keV electron beam defocused to a diameter of 30  $\mu\text{m}$ . X-ray intensities were converted to element concentrations using a CITZAF algorithm. Reference standards included a variety of silicate and oxide minerals. The sample was analyzed at  $\sim$ 10 randomly selected spots. Compositional averages are reported in Table 1 as oxide weight percent. Assuming that the melt glass major element chemistry is representative of the original host rock, the data indicate that the working point lithology for this test was a high-silica rhyolite.

Table 1. Mass percent oxide composition of JMK-3<sup>§</sup> melt glass (average based on ~10 microprobe analyses).

Oxide	Wt. %
SiO <sub>2</sub>	77.25
TiO <sub>2</sub>	0.07
Al <sub>2</sub> O <sub>3</sub>	12.56
FeO <sup>†</sup>	0.79
MnO	0.00
MgO	0.08
CaO	0.61
Na <sub>2</sub> O	3.25
K <sub>2</sub> O	5.22
<b>Total</b>	<b>99.83</b>

<sup>†</sup> Fe reported as +2 oxidation state though it is, in reality, of mixed valence.

<sup>§</sup> Analysis performed on JMK-1 glass. JMK-1 and JMK-3 glasses were taken from the same location and major element composition is expected to be the same.

For glass characterization purposes, activities and concentrations of gamma-emitting radionuclides were measured in the melt glass using a fixed Ge(Li) detector. The total count time was 1 day. Gamma spectra data were obtained for <sup>60</sup>Co, <sup>137</sup>Cs, <sup>152</sup>Eu, <sup>154</sup>Eu, <sup>155</sup>Eu, and <sup>241</sup>Am (Table 2), and reported values reflect activities at the time of data acquisition (31 January 2002). The data reveal that the melt glass is from one of the more recent NTS underground tests (probably <20 years old) as indicated by the readily detectable amounts of fission products with half-lives on the order of 5 to 10 years.

Table 2. Gamma spectroscopy results for JMK-3 melt glass.

Isotope	Half-life (years)	Concentration (atoms/g)	γ-activity (dpm/g)
<sup>60</sup> Co	5.27	$2.0 \times 10^9$	$4.9 \times 10^2$
<sup>137</sup> Cs	30.2	$1.1 \times 10^{12}$	$4.8 \times 10^4$
<sup>152</sup> Eu	13.5	$9.9 \times 10^9$	$9.6 \times 10^2$
<sup>154</sup> Eu	8.59	$2.0 \times 10^9$	$3.0 \times 10^2$
<sup>155</sup> Eu	4.71	$7.3 \times 10^8$	$2.1 \times 10^2$
<sup>241</sup> Am	433	$1.0 \times 10^{12}$	$3.1 \times 10^3$

The surface area of the glass was measured by BET (Brunauer et al., 1938) using a Micrometrics Gemini II 2370 surface area analyzer. The melt glass was outgassed under vacuum at 110°C. The JMK-3 melt glass was determined to have a surface area of 0.30 m<sup>2</sup>/gram. The specific surface area of the sample approaches the expected surface



area based on non-porous smooth spheres within the sieved particle size range (0.1 to 0.05 m<sup>2</sup>/g).<sup>1</sup> However, it is slightly higher than expected, most likely due to entrainment of smaller particles, as can be seen in SEM photos (see Figure 7). Importantly, crushed nuclear melt glass particles in the 25-53 mm size range do not appear to have significant internal porosity (no internal porosity features observed on the particle surfaces). Thus, the measured surface area of the crushed nuclear melt glass is very likely much higher than the reactive surface area of its non-crushed parent nuclear melt glass. This is consistent with lower whole-rock effective reactive surface area measurements reported by Bourcier et al. (2000) (0.001 to 0.01 m<sup>2</sup>/g) and the specific surface area measurements of the more massive obsidian glasses of Papelis et al. (2000) (0.001 to 0.05 m<sup>2</sup>/g for coarsely ground low porosity volcanic glass samples 3 and 9 and massive volcanic glass samples A and B reported in Table 3-2 of Papelis et al., 2000).

## 2.2 Scanning Electron Microscopy and X-ray Diffraction

A Hitachi S-4500 SEM which utilizes a cold field emission electron source was used to image the reacted and unreacted glass samples. Acceleration voltages of 1.3, 1.8, and 3 kV were used for imaging, depending on the charging characteristics of each sample. X-ray microanalysis was performed with a EDAX Phoenix system attached to the S-4500 at an acceleration of 6 kV. All samples were characterized without the application of conductive coatings.

X-ray diffraction scans were collected using a Scintag PAD-V generator equipped with a Cu X-ray tube operated at 45 kV and 35 mA, and a Sieffert goniometer with a solid-state detector. Diffraction patterns were collected in step scan mode at 6 seconds per 0.02° 2 $\theta$ . Collimation was provided by a 1° divergence and 2° scatter slit on the x-ray tube and a 0.3 mm scatter and 0.2 mm registration slit on the detector. Samples were scanned from 2 to 50° 2 $\theta$ .

## 3 RESULTS AND DISCUSSION

Although the original focus of these experiments was on formation of secondary minerals, little evidence of secondary mineral precipitation was observed from XRD and SEM measurements. Initial estimates of glass dissolution rates based on those in Pawloski et al. (2001) significantly overestimated the rates of glass dissolution/secondary mineral precipitation. Only small quantities of secondary minerals formed during the course of these experiments and the identity of these secondary minerals could only be qualitatively evaluated. As a result, the discussion presented below is focussed more towards providing important data regarding the *overall rates* of nuclear melt glass dissolution and subsequent secondary mineral formation and changes in solution composition as a function of temperature. As described in the Introduction, the changes

---

<sup>1</sup> Papelis et al. (2000) found that surface areas of material with crushed particles sizes near 10  $\mu$ m approach the expected surface area based on non-porous smooth spheres.

in the fluid composition in contact with dissolving melt glass and precipitating secondary minerals will greatly affect glass dissolution rates. Solution chemistry data can also provide qualitative evidence regarding the identity of dominant secondary minerals.

### 3.1 Solution Conditions

ICP-AES was used to analyze solutions for Al, Ca, K, Mg, Na, and Si at the end of batch dissolution experiments. Results are shown in Table 3. Eh and pH were measured using a platinum combination redox electrode and a combination pH electrode, respectively. Results from the Eh and pH measurements are listed in Table 4. All measurements were made on samples collected after the reaction vessels were removed from ovens and allowed to cool for ~2 days. Some changes in the solution composition may have occurred during cooling, particularly for the high temperature experiments; the values may, therefore, not accurately represent the solution composition at temperature (see Knauss and Peifer, 1986). To calculate the pH at temperature, the measured pH (25°C) and solution composition was input into the Geochemist's Workbench geochemical modeling code and recomputed to the desired temperature.<sup>2</sup> The resulting pH at temperature is reported in Table 4. The pH (at temperature) tends to decrease with increasing temperature (and, presumably, increasing glass dissolution and secondary mineral precipitation). However, very dramatic changes in pH are not observed at any temperature. This suggests that the pH excursion in the clay-dominating secondary precipitate simulation illustrated in Figure 1 is not likely. Interestingly, because the pH of neutrality tends to decrease with temperature, the pOH (or alkalinity) is actually higher in the 80-200°C experiments than in the 40°C experiment.

Table 3. Elemental composition of post reaction solutions.

Sample #	Al	Ca	K	Mg	Na	Si
	----- mg/kg -----					
JMK-3 40°C	<i>n.d.</i>	1.20	5.2	0.038	140	29
JMK-3 80°C	0.29	1.40	5.8	0.044	140	130
JMK-3 120°C	0.31	1.40	5.8	0.039	140	180
JMK-3 160°C	0.91	0.93	7.0	0.029	130	250
JMK-3 200°C	0.57	1.10	6.4	0.026	130	170

*n.d.* – below instrument detection limit

<sup>2</sup> The GEMBOCHS thermodynamic database of Johnson and Lundeen (1997) was used. Mineral precipitation was suppressed.

Table 4. Reaction time, Eh and pH of post reaction solutions.

Sample #	Reaction time (days)	Eh, volts	pH	pH at T	pOH at T <sup>a</sup>
JMK-3 40°C	88	0.213	8.95	8.76	4.78
JMK-3 80°C	88	0.179	9.54	8.73	3.87
JMK-3 120°C	111	0.191	9.60	8.27	3.69
JMK-3 160°C	111	0.056	8.10	7.61	3.94
JMK-3 200°C	111	0.049	7.77	7.63	3.66

<sup>a</sup> Because the solution pH of neutrality decreases with increasing temperature, pH + pOH decreases with temperature. Comparison of pH to pOH can be used to evaluate the alkalinity of the solution.

### 3.1.1 SiO<sub>2</sub>(aq) in Solution

Notwithstanding the possible changes in solution chemistry during sample cooling, it is interesting to compare the measured Si concentrations to the solubilities of several silica minerals (Figure 2). All data fall below the solubility of amorphous SiO<sub>2</sub>, consistent with the hypothesis that amorphous SiO<sub>2</sub> can be used as the solubility limiting phase of glass. The Si concentration in solution was between that of  $\beta$ -cristobalite and  $\alpha$ -cristobalite solubility between 40 and 160°C and was below that of  $\alpha$ -cristobalite at 200°C. This suggests that  $\beta$ -cristobalite limits Si concentrations between 40 and 160°C while  $\alpha$ -cristobalite may limit Si concentrations at 200°C. However, because data were not taken as a function of time to evaluate whether steady state had been reached, we cannot be sure that the solution composition measured at the end of these batch sorption experiments represents steady state solution conditions. Furthermore, some aqueous Si may have precipitated during sample cooling which would skew the data to lower aqueous Si concentrations. Knauss and Peifer (1986) observed a 40% loss in Si from solution as a result of quenching for their 250°C vitric tuff dissolution experiments. However, they observed relatively small losses at 150 and 90°C. In the context of the data presented here, it suggests that the relatively low aqueous Si concentrations at 200°C may, in part, be the result of precipitation during cooling. At the lower temperatures, it is less likely that aqueous Si was lost due to precipitation during sample cooling.

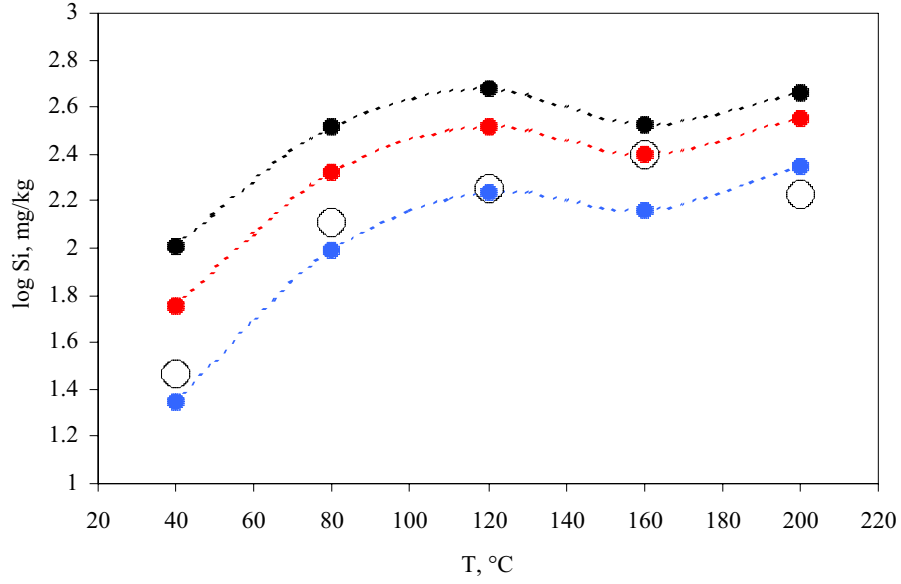


**Figure 2. Si concentration as a function of temperature from batch glass reaction experiments compared to the calculated solubility of amorphous SiO<sub>2</sub>, α-cristobalite, and β-cristobalite based on solution conditions described in Tables 3 and 4.**

The aqueous Si concentration in the 40°C sample is significantly lower than the solubility of amorphous SiO<sub>2</sub> and also β-cristobalite, suggesting that we may not have reached steady state by the end of the 3-month batch experiment. We can simulate the buildup of aqueous Si in our experiments using the transition-state-theory (TST) glass dissolution rate model used recently in CHESHIRE simulations (Pawloski et al., 2001):

$$r = k_0 \times e^{\frac{E_a}{R} \left( \frac{T - T_0}{T_0 T} \right)} \times A_s \times \prod_i a_i^{n_i} \times \left( 1 - \left( \frac{Q}{K} \right)^{1/\sigma} \right)^v + A_s k_f \quad (1)$$

where  $r$  is the rate of glass dissolution (mol-glass g<sup>-1</sup> sec<sup>-1</sup>),  $k_0$  is the far-from-saturation glass dissolution rate (mol-glass m<sup>-2</sup> sec<sup>-1</sup>) at temperature  $T_0$ ,  $E_a$  is the activation energy (cal mol<sup>-1</sup>) which accounts for the change in glass dissolution as a function of temperature,  $R$  is the gas constant (1.99 cal mol<sup>-1</sup> K<sup>-1</sup>),  $T$  and  $T_0$  are the temperature of interest and the reference temperature (typically 25°C), respectively,  $A_s$  is the surface area of the glass (m<sup>2</sup> g<sup>-1</sup>),  $a_i^{n_i}$  are a series of dissolution-inhibiting or -promoting solution aqueous species activities taken to the  $n$ th power,  $Q$  is the saturation of the solution relative to the solubility product of the glass ( $K$ ). The term  $\sigma$  is related to the stoichiometry of the rate-limiting reaction step but is generally fitted empirically. The term  $v$  is an empirical term often added to dissolution/precipitation model (e.g. Bourcier et al., 1994). Finally,  $k_f$  is the close-to-saturation term (mol-glass g<sup>-1</sup> sec<sup>-1</sup>), which is

included to account for dissolution very close to saturation resulting from the inherent instability of glasses (Grambow, 1987). In the CHESHIRE model of Pawloski et al. (2001), the  $\sigma$ ,  $\nu$ , and close-to-saturation terms were ignored. The activation energy was set to 20 kcal/mol,  $Q$  was set by the aqueous activity of  $\text{SiO}_2(\text{aq})$ ,  $K$  was set by the solubility of amorphous  $\text{SiO}_2$ , and the rate constant and affinity terms were of the following form:

$$k_0 \times \prod_i a_i^{n_i} \approx 10^{-11.59} + 10^{-8.01} \times (\text{OH}^-)^{0.5155} + 10^{-9.51} \times (\text{H}^+)^{0.4566} \quad (2)$$

The predicted buildup of aqueous Si in our experiments based on the CHESHIRE glass model is shown in Figure 3.<sup>3</sup> Our recent experimental measurements of glass dissolution close to saturation (Zavarin et al., 2004) resulted in several changes to the CHESHIRE glass model of Pawloski et al. (2001); predictions based on this model are included in Figure 3 as well. In this modified model, the close to saturation term was ignored while the  $\sigma$  term was set to 100 ( $\nu$  term not used). The activation energy was set to 12 kcal/mol, the  $Q$  and  $K$  terms were treated as before, and the rate constant and affinity terms were of the following form:<sup>4</sup>

$$k_0 \times \prod_i a_i^{n_i} \approx 10^{-11.33} + 10^{-8.28} \times (\text{OH}^-)^{0.5519} + 10^{-9.24} \times (\text{H}^+)^{0.4825} \quad (3)$$

For the 40°C experiment at 88 days (the end of the experiment), the predicted Si concentration in solution is 76 and 18 ppm for the CHESHIRE model and modified CHESHIRE model, respectively, compared to 29 ppm from the experiment. Unlike the original model, the modified CHESHIRE glass dissolution model appears to predict the rate of glass dissolution (and Si buildup) rather well. It also suggests that glass dissolution at 40°C is slow enough that, over 88 days, loss of Si from solution due to mineral precipitation was unlikely.<sup>5</sup> At 80°C, the modified CHESHIRE glass dissolution model predicts that the aqueous Si concentration would reach 131 ppm at 88 days (compared to the observed value of 130 ppm). Again, a steady state was not reached (see Figure 2), suggesting that significant secondary mineral precipitation was unlikely. For the 120 to 200°C experiments, glass dissolution rates are predicted to be fast enough so that some

---

<sup>3</sup> The buildup of Si in solution was simulated assuming that secondary minerals do not precipitate. This is likely to be the case while the solutions are undersaturated with respect to the cristobalite phases but is increasingly less likely as the buildup of Si increases.

<sup>4</sup> The rate constant and affinity terms differ slightly from the model of Pawloski et al. (2001) due to subtle improvements to the original data fitting. However, the effect is rather minor.

<sup>5</sup> If the modified glass dissolution model, excluding any secondary mineral precipitation, accurately predicts the buildup of Si in solution, it is likely that significant amounts of Si-bearing secondary minerals have not precipitated. If the modified glass dissolution model, excluding any secondary mineral precipitation, overestimates Si buildup in solution, either secondary mineral precipitation may have reduced Si concentrations.

secondary minerals are likely to form.<sup>5</sup> Identification of secondary minerals, based on examination of the solution chemistry, is discussed below. Identification of secondary minerals from SEM and XRD measurements is discussed in Section 3.3.

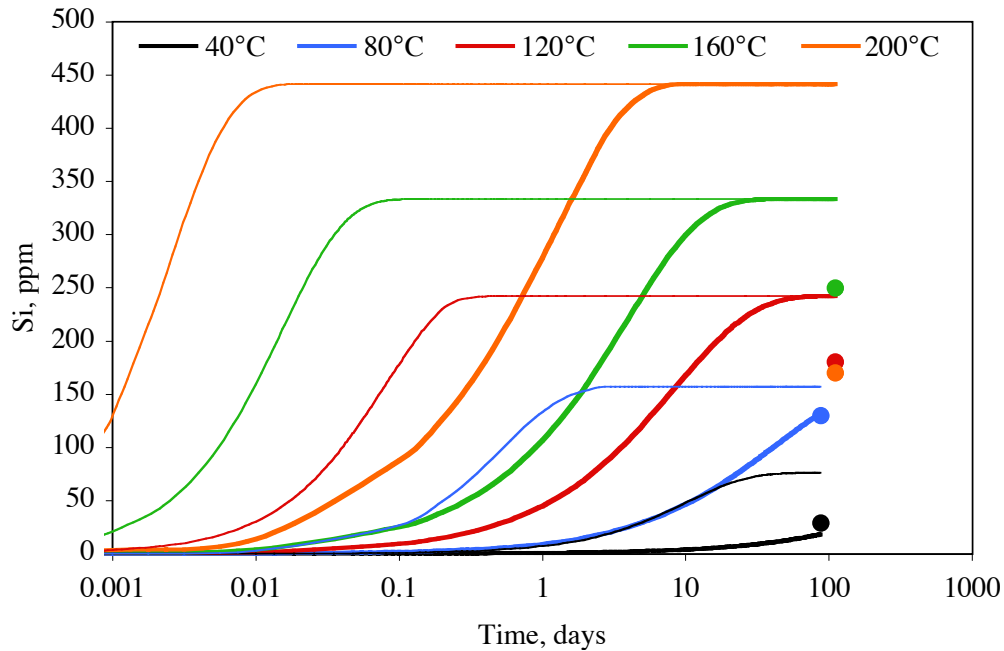


**Figure 3. Predicted buildup of Si in solution as a function of time for batch glass reaction experiments from 40 to 200°C (ignoring secondary mineral precipitation): the CHESHIRE model of Pawloski et al. (2001) (thin lines), the modified CHESHIRE model of Zavarin et al. (2004) (thick lines), and measured data (circles).**

### 3.1.2 Saturation State of Solutions

The data in Table 3 and 4 can be used to examine the solution saturation state with respect to various minerals as a function of temperature. This provides some indirect evidence as to the possible mineral phases controlling the activity of aqueous species. Table 5 lists the saturation state of solutions with respect to a number of minerals typically observed in devitrified tuffs of Pahute Mesa.<sup>6</sup>

Feldspars are commonly the dominant mineral found in devitrified tuffs of Pahute Mesa (see Warren et al., 2000, database). Feldspars generally form at high temperatures as part of the devitrification process in rhyolite glasses. Holler and Wirsching (1976)

<sup>6</sup> Since the nuclear melt glass is compositionally very similar to the natural glasses which were the precursors to the devitrified tuffs at Pahute Mesa, it is likely that the secondary precipitates resulting from the dissolution of nuclear melt glass will be similar to those found in the devitrified tuffs at Pahute Mesa.

found that alkali feldspars formed during rhyolite glass dissolution at temperatures above 200°C. Our modeling results suggest that solutions held at 200°C were in equilibrium with K-feldspar while solutions held at lower temperatures were supersaturated. This suggests that the solution composition may be controlled, in part, by K-feldspar solubility at temperatures of 200°C and above. At lower temperatures, K-feldspar precipitation may be kinetically limited.

All solutions are close to equilibrium with calcite. This should not be surprising given the typically fast dissolution/precipitation rates of calcite, its stability over a wide range of temperatures, and its ubiquitous distribution in the environment.

Smectite is a common secondary mineral formed during dissolution of rhyolite glasses (Holler and Wirsching, 1976). The term smectite is used to identify a variety of clay minerals of similar structure (sometimes also called the montmorillonite group of minerals). These include nontronite (a dioctahedral Fe-rich member), beidellite (an dioctahedral Al-rich member), montmorillonite (a dioctahedral Mg-rich member), saponite (a trioctahedral Mg-rich member), and others. Moreover, each of the individual varieties has a significant number of ion exchange sites; these sites may be occupied by a number of cations, each of which represents an end member in and of itself. The complex nature of the smectite minerals creates difficulty in modeling this chemically variable mineral group. Evaluating the saturation state of solutions with respect to each end-member provides the simplest method for examining the saturation state of solutions with respect to this group of minerals. In Table 5, a range of saturation for each variety of smectite is listed. The range of saturation for each variety relates to the counter ion associated with the ion exchange sites. In general, the lowest saturation is associated with the monovalent  $K^+$  exchanged smectite while the highest saturation is associated with the divalent  $Ca^{2+}$  exchanged smectite.

The saturation state with respect to saponite is not listed in Table 5 but all solution are highly supersaturated with respect to this mineral. Precipitation of this end-member smectite appears to be kinetically limited. Solutions are supersaturated with respect to nontronite as well. This would suggest that precipitation of this end member smectite is inhibited or kinetically limited. However, because the total  $Fe^{3+}$  in solution was not measured, we based our  $Fe^{3+}$  concentrations on an assumed solution saturation with goethite. If  $Fe^{3+}$  in solution was predicted to be controlled by a lower solubility iron oxide such as hematite, the solutions would still be supersaturated but would begin to approach saturation with respect to nontronite.

Unlike in the case of iron-rich nontronite and trioctahedral Mg-rich saponite, solutions at all temperatures appear to be close to saturation with respect to Al-rich beidellite. Solutions are either under- or over-saturated but within 2 log units of equilibrium. This suggests that beidellite may precipitate and, in part, control solution composition in contact with melt glass over a wide temperature range. It also suggests that beidellites may be a common secondary precipitate that forms as a result of glass dissolution.

Solutions are supersaturated with respect to montmorillonite but not as severely as for nontronite. In particular, at 200°C, the solution appears to be approaching equilibrium with montmorillonite. At lower temperatures, solution are significantly more supersaturated.

It is important to remember that montmorillonite, beidellite, saponite, and nontronite represent end-members of the smectite group of minerals. None of these end-members are likely to form as a result of nuclear melt glass dissolution. More likely is the formation of a mixed smectite whose solubility will differ from its end-members. However, a mixing model that would accommodate variations in the framework and ion exchange site composition is not available. As an example, we examined the saturation state of solutions with respect to two smectite minerals described as “high Fe/Mg” and “low Fe/Mg”. These mineral compositions were based on samples collected in basaltic rock and are, therefore, not likely to be representative of smectite compositions at Pahute Mesa. Nevertheless, interestingly, the saturation state of solutions with respect to either of these smectite minerals is close to equilibrium, particularly in the “high Fe/Mg” case. These results, and the modeling results for end-member smectites, suggests that solutions at all temperatures examined are close to saturation with respect to some smectite clays. Of the end-member smectites, beidellite solubility equilibrium most closely matches the solution compositions at all temperatures.

In the case of SiO<sub>2</sub> solubility, most solutions appear to be between saturation with respect to  $\alpha$ -cristobalite and  $\beta$ -cristobalite, suggesting that  $\beta$ -cristobalite is a reasonable SiO<sub>2</sub> solubility limiting phase. However, glass dissolution rate predictions suggest that solutions at 40 and 80°C may not have reached steady state. At 200°C, SiO<sub>2</sub> concentrations suggest that  $\alpha$ -cristobalite may be the solubility limiting phase. However, silica precipitation during sample cooling may have reduced SiO<sub>2</sub> aqueous concentrations, as described earlier.

The saturation state with respect to mica (represented by illite and muscovite) is close to equilibrium at all temperatures. Illite is often observed as an interlayered mixture with smectites. Its saturation condition follows that of beidellite and montmorillonite minerals in these solutions. Solutions are close to saturation or somewhat undersaturated with respect to kaolinite. Kaolinite was observed as a secondary mineral product of rhyolite glass dissolution at 250°C in Holler and Wirsching (1976).

The saturation state of solutions with respect to several zeolites is reported in Table 5. Analcime, clinoptilolite, and mordenite have all been observed in Pahute Mesa devitrified tuffs. However, the clinoptilolite abundance in devitrified tuffs is more than ten times that of mordenite or analcime (data of Warren et al., 2000). Solutions are supersaturated with respect to all three zeolites below 200°C. Clinoptilolite appears to be the more stable of the three in the lower temperature solutions. The fact that solutions are supersaturated with respect to clinoptilolite suggest that this mineral was not controlling solution composition, possibly as a result of kinetic limitations. The stability of clinoptilolite over the other zeolites suggests that this zeolite might eventually form at the



lower temperatures. The fact that the stability of analcime compared to clinoptilolite increases with temperature is consistent with estimates of Chipera et al. (1995) for Yucca Mountain waters. The formation of analcime at 200°C and above was observed in closed system rhyolite glass dissolution experiments of Holler and Wirsching (1976). Mordenite tended to form at the lower temperatures (~150°C). Interestingly, Holler and Wirsching (1976) did not report any clinoptilolite formation in their rhyolite glass dissolution experiments. Knauss (1987), on the other hand, found that clinoptilolite was the dominant secondary mineral formed during 250°C dissolution experiments of vitric tuffs from Yucca Mountain.

Table 5. Minerals observed in devitrified tuffs of Pahute Mesa and their state of saturation in glass dissolution experiments.

Minerals observed in Pahute Mesa Tuffs	Minerals included in model	Model Temperature, °C <sup>a</sup>			
		80	120	160	200
		Saturation State, log(Q/K)			
feldspar	K-feldspar $\text{KAlSi}_3\text{O}_8$	2.5	1.2	1.8	-0.1
calcite, dolomite	calcite $\text{CaCO}_3$	0.4	0.5	0.3	0.7
	nontronite <sup>b</sup> $(\text{Ca/Mg/Na/K})\text{Fe}_2\text{Al}_{0.33}\text{Si}_{3.67}\text{O}_{10}(\text{OH})_2$	4.2 to 4.7	3.3 to 3.9	3.8 to 4.6	2.3 to 3.1
	beidellite <sup>b</sup> $(\text{Ca/Mg/Na/K})\text{Al}_{2.33}\text{Si}_{3.67}\text{O}_{10}(\text{OH})_2$	0.4 to 0.9	-1.6 to -0.9	1.0 to 1.8	-2.1 to -1.2
smectite <sup>c</sup>	montmorillonite <sup>b</sup> $(\text{Ca/Mg/Na/K})\text{Mg}_{0.33}\text{Al}_{1.67}\text{Si}_4\text{O}_{10}(\text{OH})_2$	2.4 to 2.9	0.9 to 1.5	2.5 to 3.2	-0.1 to 0.7
	smectite,high Fe/Mg $\text{Ca}_{0.025}\text{Na}_{0.1}\text{K}_{0.2}\text{Fe}^{2+}_{0.5}\text{Fe}^{3+}_{0.2}\text{Mg}_{1.15}\text{Al}_{1.25}\text{Si}_{3.5}\text{O}_{10}(\text{OH})_2$	-0.5	-0.9	1.0	-0.3
	smectite,low Fe/Mg $\text{Ca}_{0.02}\text{Na}_{0.15}\text{K}_{0.2}\text{Fe}^{2+}_{0.29}\text{Fe}^{3+}_{0.16}\text{Mg}_{0.9}\text{Al}_{1.25}\text{Si}_{3.75}\text{O}_{10}(\text{OH})_2$	1.2	0.5	1.8	0.2
cristobalite, tridymite, quartz,	$\alpha$ -cristobalite $\text{SiO}_2$	0.1	0.0	0.2	-0.1
glass, opal	$\beta$ -cristobalite $\text{SiO}_2$	-0.2	-0.3	0.0	-0.3
kaolinite	kaolinite $\text{Al}_2\text{Si}_2\text{O}_5(\text{OH})_4$	0.1	-1.6	0.5	-2.0
mica	illite $\text{K}_{0.6}\text{Mg}_{0.25}\text{Al}_{1.8}\text{Al}_{0.5}\text{Si}_{3.5}\text{O}_{10}(\text{OH})_2$	2.0	0.1	2.0	-0.9
	muscovite $\text{KAl}_3\text{Si}_3\text{O}_{10}(\text{OH})_2$	2.5	-0.1	2.2	-1.2
analcime	analcime $\text{Na}_{0.96}\text{Al}_{0.96}\text{Si}_{2.04}\text{O}_6 \cdot \text{H}_2\text{O}$	1.1	0.3	0.8	-0.4
clinoptilolite <sup>d</sup>	clinoptilolite $(\text{Ca/Na/K})\text{Al}_{3.45}\text{Fe}_{0.017}\text{Si}_{14.533}\text{O}_{36} \cdot 10.922 \text{H}_2\text{O}$	4.2 to 8.9	-1.0 to 5.8	0.8 to 9.2	-7.2 to 2.6
mordenite	mordenite $\text{Ca}_{0.289}\text{Na}_{0.361}\text{Al}_{0.94}\text{Si}_{5.06}\text{O}_{12} \cdot 3.468 \text{H}_2\text{O}$	1.9	0.8	1.9	-0.4
hematite <sup>e</sup> , hornblende, gypsum					

<sup>a</sup> 40°C data not included because Al concentration was below the detection limit.

<sup>b</sup> Ca, Mg, Na, and K end members examined. Their proportions in the end member minerals is  $\text{Ca}_{0.165}$ ,  $\text{Mg}_{0.165}$ ,  $\text{K}_{0.33}$ , or  $\text{Na}_{0.33}$ .

<sup>c</sup> Smectite is a general term for a type of layered clay. Smectites include nontronite, beidellite, montmorillonite, and saponite. All these minerals were examined in the modeling effort. Saponite<sup>b</sup>,  $(\text{Ca/Mg/Na/K})\text{Mg}_3\text{Al}_{0.33}\text{Si}_{3.67}\text{O}_{10}(\text{OH})_2$ , was highly supersaturated in all cases.

<sup>d</sup> Ca, Na, and K end members examined. Their proportions in the end member minerals is  $\text{Ca}_{1.7335}$ ,  $\text{Na}_{3.467}$ , or  $\text{K}_{3.467}$ .

<sup>e</sup> Fe concentrations were not measured in solution. In our modeling effort,  $\text{Fe}^{2+}$  and  $\text{Fe}^{3+}$  concentrations were controlled by assuming saturation with goethite ( $\text{FeOOH}$ ) and the proportion of  $\text{Fe}^{2+}$  and  $\text{Fe}^{3+}$  controlled by the Eh of the solution.

### 3.1.3 Redox State of Solutions

The Eh of solutions exposed to dissolving glass at various temperatures was measured at the end of each experiment (i.e. once solutions had cooled to 25°C).<sup>7</sup> Interestingly, the solutions reacted at 40, 80, and 120°C have a significantly higher Eh (~200 mV) compared to the 160 and 200°C solutions (~50 mV). The results suggest that the dissolution of significant amounts of melt glass may result in a more reducing environment in the glass zone. The solution redox conditions are overlayed on an Eh-pH diagram (Figure 4) for the  $\text{Fe}^{2+}/\text{Fe}^{3+}$  system at 25°C. This comparison suggests that at higher temperatures (where glass dissolution rates are relatively fast), the Eh may be controlled by  $\text{Fe}^{2+}$  in solution that results from its release from the melt glass. Recent redox state measurements of nuclear melt glass (Allen et al., 2003), have reported that between 33 and 53% of Fe in the nuclear melt glasses examined was in the  $\text{Fe}^{2+}$  state. This suggests that a significant source of  $\text{Fe}^{2+}$  may be available to provide somewhat reducing conditions where glass is dissolving.<sup>8</sup> In Figure 5, the batch experiment Eh-pH data are overlayed on a Pu redox speciation diagram. In addition, the Eh-pH condition used in the CHESHIRE model of Pawloski et al. (2001) is plotted. The results suggest that glass dissolution will tend to result in reducing conditions that favor the stability of the +4 oxidation state of Pu. This has significant ramifications to the transport behavior of Pu since the +4 oxidation state sorbs much more strongly to mineral surfaces (including mineral colloid surfaces) than the +5 state. When compared to the conservative redox condition used in the CHESHIRE model (Pawloski et al., 2001), it suggests that significantly greater Pu sorption to fracture-lining and matrix minerals as well as colloids may occur. However, it is important to note that mixing of the reducing waters from the glass zone with ambient groundwater from near the cavity may buffer the redox state of near-field groundwater.

---

<sup>7</sup> We did not attempt to predict Eh at the reaction temperature

<sup>8</sup> Note that this may occur at high and low temperatures. However, at low temperatures, glass dissolves much more slowly and, as a result, less  $\text{Fe}^{2+}$  is available to affect the Eh.

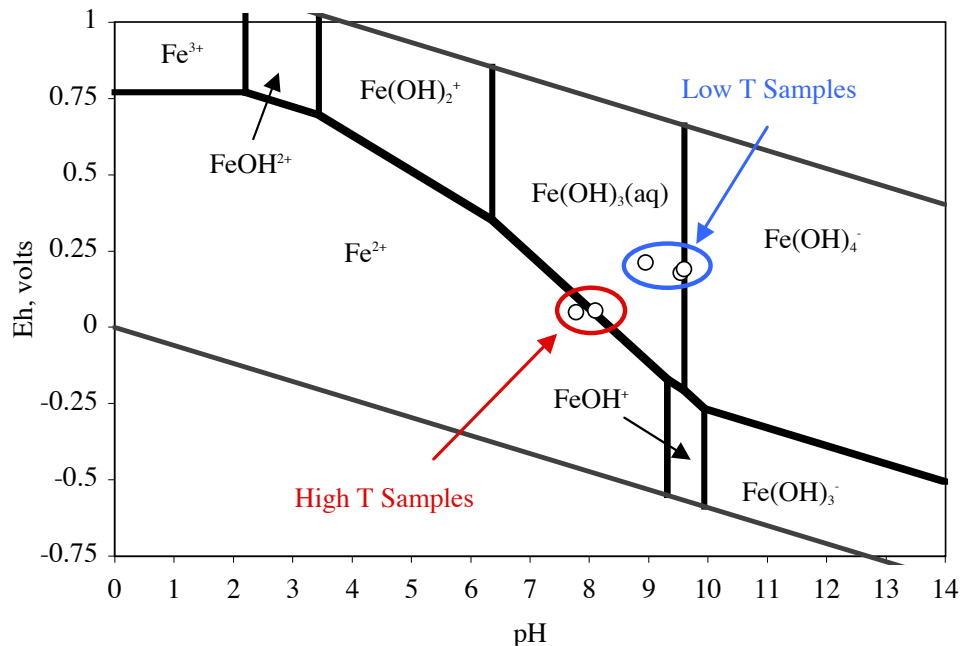


**Figure 4.** Eh and pH data (at 25°C) from reacted glasses on an Eh – pH diagram of Fe (25°C). Low T samples include 40, 80, and 120°C solutions; high T samples include 160 and 200°C solutions.

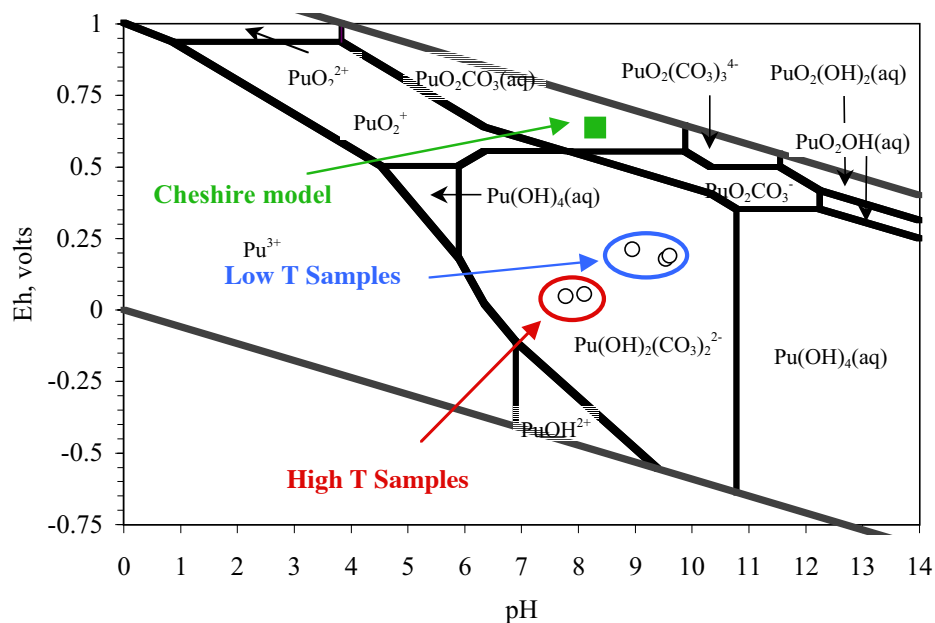


**Figure 5.** Eh and pH data (at 25°C) from reacted glasses and CHESHIRE model condition on an Eh – pH diagram of Pu (25°C). Low T samples include 40, 80, and 120°C solutions; high T samples include 160 and 200°C solutions.  $\text{HCO}_3^-$  activity set to  $10^{-2.6}$  (predicted  $\text{HCO}_3^-$  activity at pH ~8).

### 3.2 Predicted Glass Dissolution Rates

Although some solution conditions reported in Tables 3 and 4 (particularly the 40°C and 80°C samples) may not represent steady state conditions, it is useful to qualitatively evaluate the predicted glass dissolution (and secondary mineral precipitation) rates based on these solution conditions.<sup>9</sup> In Figure 6, we plot the simulated percent glass dissolution as a function of time for each experiment assuming the solutions sampled at the end of the batch experiments (i.e. Tables 3 and 4 solution conditions) represent the steady state condition. The glass dissolution model was based either on the CHESHIRE model (Pawloski et al., 2001) or the modified CHESHIRE model (Zavarin et al., 2004). The rate of glass dissolution is much faster with the CHESHIRE model than with the modified model. This is consistent with the results reported in Zavarin et al. (2004) which showed an order of magnitude difference in glass dissolution between the two models at 40°C and a three order of magnitude difference at 160°C. At 200°C, the CHESHIRE model predicts glass to dissolve completely in several days while the modified glass model predicts ~40% of the glass will dissolve in 100 days. The CHESHIRE model predicts all or nearly all of the glass will dissolve at 160 and 120°C over 100 days. This is in contrast to the modified glass model, which predicts that 4% or less of the glass will dissolve in the 160°C and lower temperature samples. These simulation results can be compared to SEM and XRD results reported in the following sections to constrain predicted glass dissolution rates.

---

<sup>9</sup> In the 120, 160 and 200°C samples, the predicted rates are likely to be conservative (i.e., faster than the actual rates) because some aqueous Si may have been lost during sample quenching. Thus, predicted rates would be based on solution conditions that are farther from saturation than in reality. In the 40 and 80°C samples, predicted rates may not be conservative because steady state was very likely not reached and solutions were much more undersaturated at early time. Thus predicted rates would be based on solution conditions that are closer to saturation than the time-integrated average saturation.

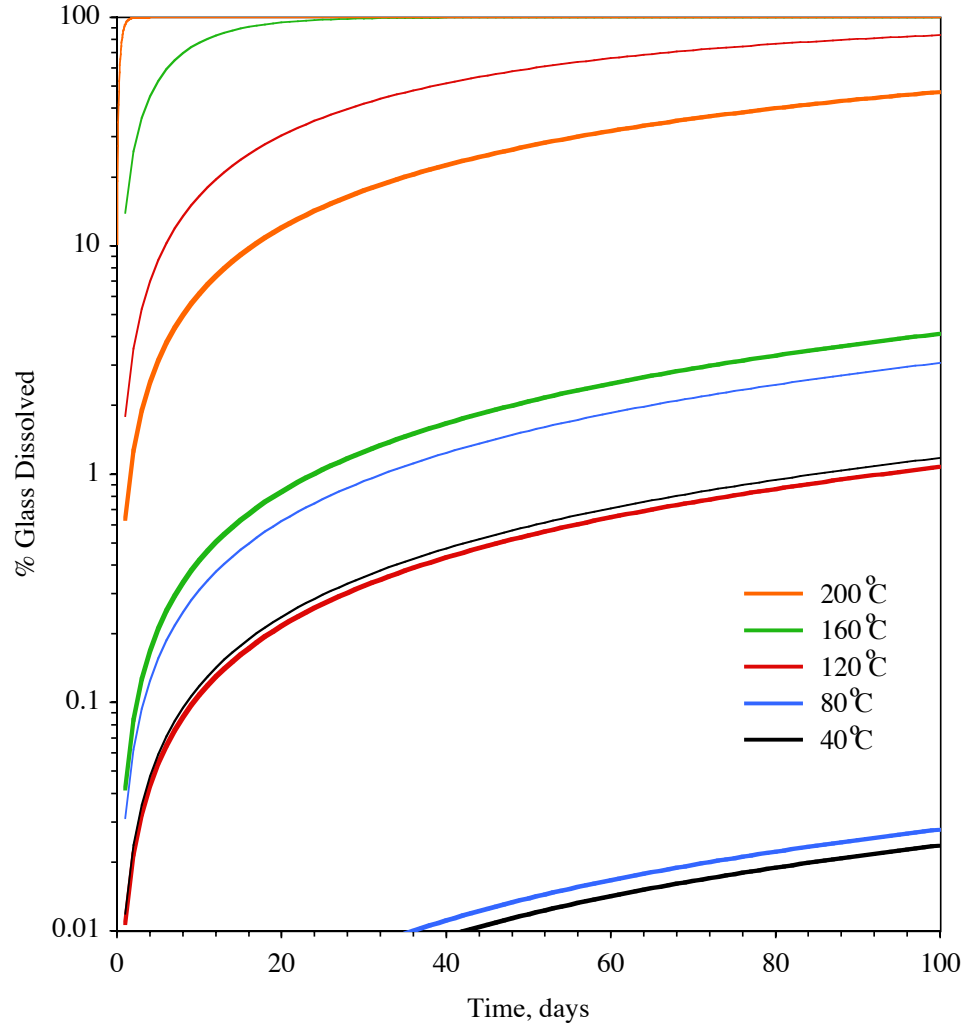


**Figure 6. Predicted glass dissolution as a function of time for solution experiments from 40 to 200°C. Thin lines represent prediction based on the CHESHIRE model (Pawloski et al., 2001). Thick lines represent prediction based on the modified CHESHIRE model (Zavarin et al., 2004).**

### 3.3 Identification of Secondary Minerals

We used x-ray diffraction and scanning electron microscopy to identify secondary minerals produced in the glass reaction tests. Based on the quantity of secondary minerals observed, we could also qualitatively estimate the rates of glass dissolution and secondary mineral precipitation. We summarize these results in the following sections and compare them with model simulations. Additional SEM photomicrographs not discussed here are included in the Appendix.

#### 3.3.1 Scanning Electron Microscopy

The unreacted nuclear melt glass was found to be composed of  $\sim 50\ \mu\text{m}$  particles as expected based on the sieving analysis (Figure 7A). At this particle size, the surface area should be  $0.05\text{--}0.1\ \text{m}^2/\text{g}$  in contrast to BET measurements of  $0.3\ \text{m}^2/\text{g}$ . The difference in surface area most likely results from the fine-grained material which appears to be attached to the larger  $50\ \mu\text{m}$  particles. This fine-grained material could not be identified by its morphology and may simply be fine-grained glass fragments that were not removed by the sample preparation procedure. The fine-grained material is distinctive in its subangular blocky character (Figure 7B).

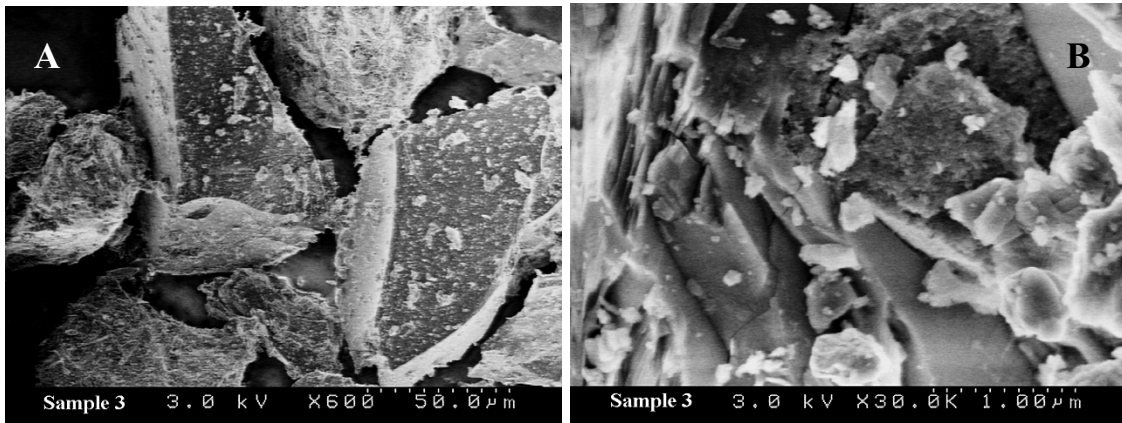


**Figure 7. SEM photomicrographs of unreacted nuclear melt glass (sample JMK-3).**

Nuclear melt glass reacted at 80°C (and, presumably, at 40°C as well) showed little or no alteration of the glass surfaces (Figure 8). However, it is interesting to note that, at all temperatures, glass particles appear to have two distinct surface morphologies (Figure 8A). Certain particle surfaces appear as freshly cleaved glass with little or no surface roughness or appearance of fine-grained material. Other particle surfaces appear with significant surface roughness and/or attached fine-grained material (Figure 8B).

In one case, a region on an 80°C reacted particle appeared to have rod-like secondary precipitate formation on the surface (Figure 8C). However, this was not consistently observed on all particle surfaces. Based on SEM observations, it appears that only slight dissolution of glass and secondary mineral precipitation occurred over several months at 80°C. This is consistent with predictions, based on the modified glass model of Zavarin et al. (2004), that less than 0.1% of the glass is likely to have dissolved and produced secondary minerals.

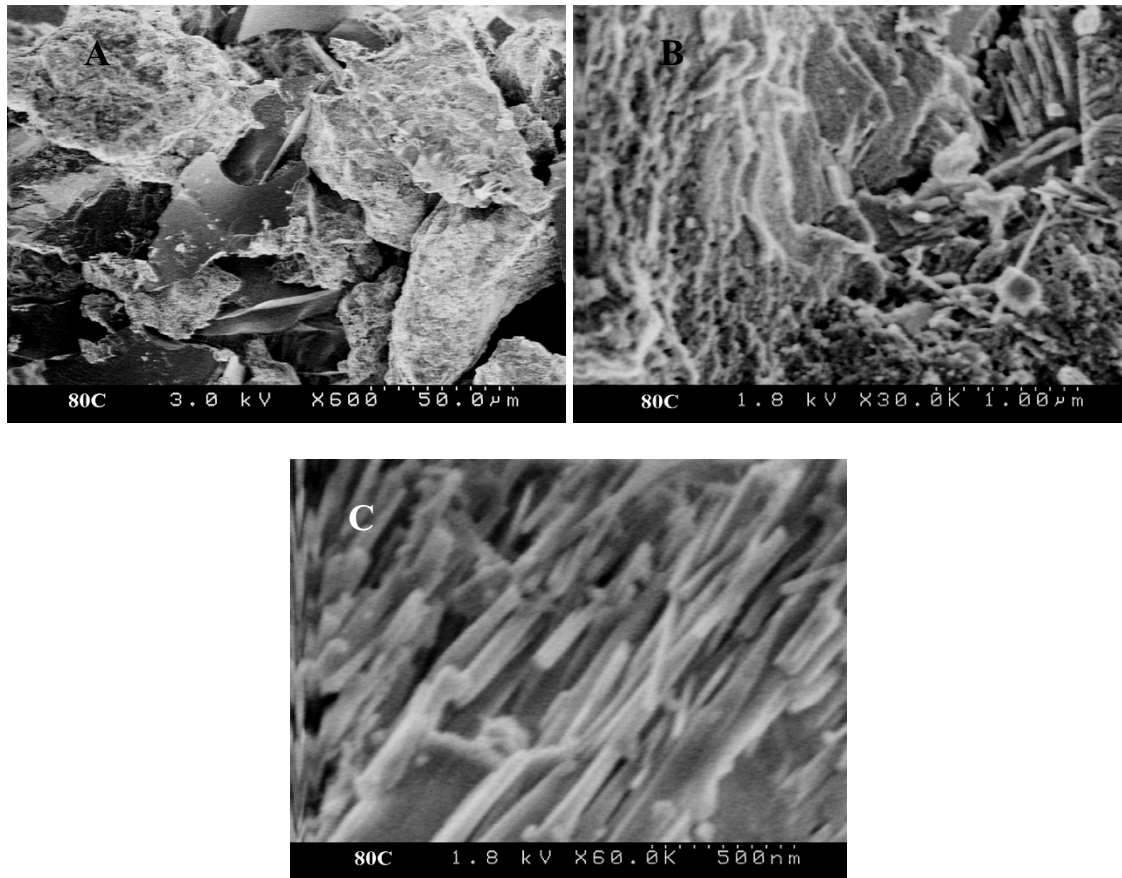


**Figure 8. SEM photomicrographs of nuclear melt glass reacted at 80°C.**



At 120°C, signs of glass dissolution and the formation of secondary minerals are significantly more prominent compared to the lower temperatures. While the appearance of the melt glass particles has not changed dramatically (Figure 9A), signs of glass dissolution at the edges of particles are visible (Figure 9B). Interestingly, while the edges of some surfaces appear to be dissolving, some surfaces retain their unreacted morphology. The heterogeneous behavior of glass dissolution indicates that certain glass surfaces are more prone to dissolution than others. This may be indicative of residual strain or heterogeneous element distribution within the glass, which provides preferential reaction along certain particle boundaries.

At 120°C, small areas with secondary mineral precipitates in the shape of  $\sim 0.1 \mu\text{m}$  rods are significantly more prevalent than at 80°C (Figure 9C). Due to their small size, an accurate chemical composition of these rod-shaped secondary minerals could not be determined. At all temperature and in nearly all cases, elemental analysis of secondary minerals yielded major element compositions similar to that of the underlying nuclear melt glass. In only one case, a particle that appeared to be a pure silica phase (most likely amorphous silica or cristobalite) was observed.

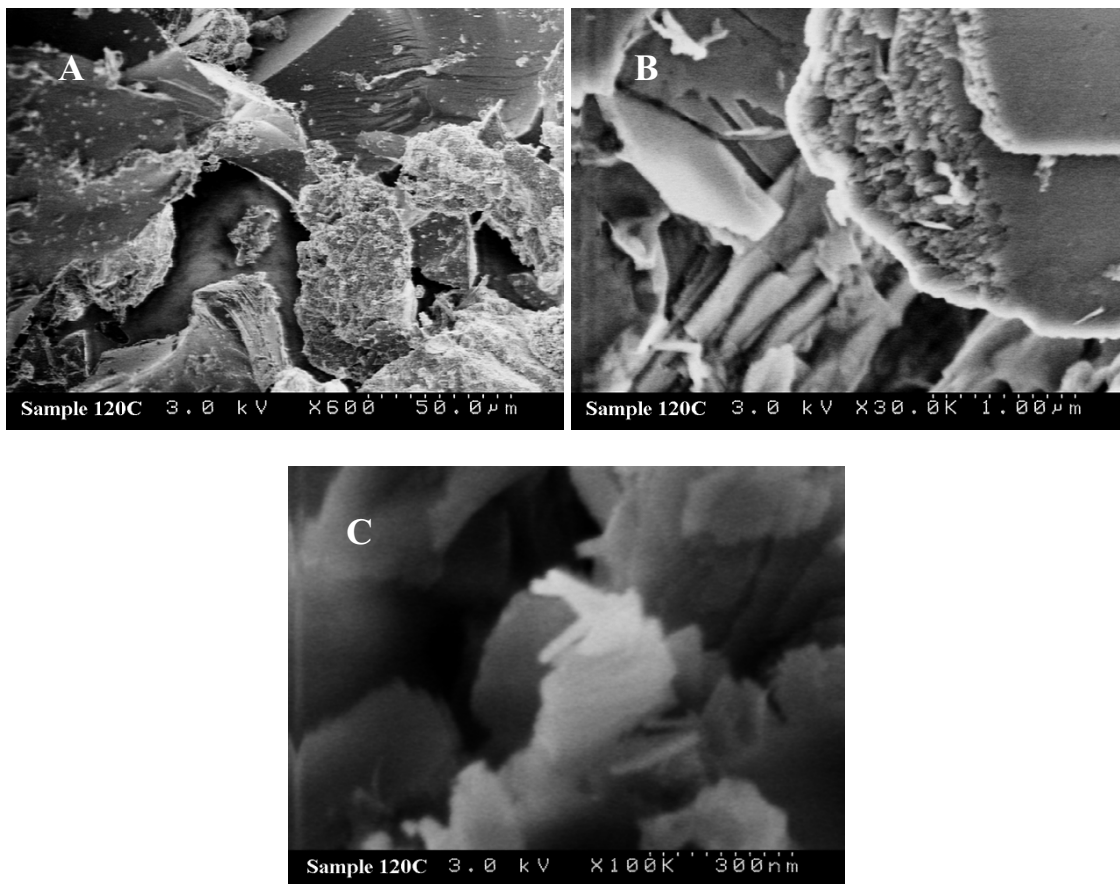


**Figure 9. SEM photomicrographs of nuclear melt glass reacted at 120°C.**

At 160°C, the overall morphology of the particles remains similar to the lower temperature samples, with certain glass surfaces appearing like freshly cleaved glass while other surfaces appear to have significantly more texture (Figure 10A). However, upon close examination, the signs of glass dissolution and secondary mineral precipitation are unmistakable. Dissolution patterns appear as steps or linear features indicating preferential dissolution in certain directions (Figures 10B and 10D). A mat of secondary mineral precipitates forms on certain glass surfaces (Figure 10C). The mat is composed of  $\sim 0.15 \times 0.6 \mu\text{m}$  elongated particles with relatively consistent morphology. A similar morphology is observed in the 200°C samples described below.

Based on the CHESHIRE glass dissolution model (Pawloski et al., 2001), we would predict that all the glass would dissolve in less than 40 days under these conditions. This is clearly not the case. SEM photomicrographs indicate that the majority of glass remains intact. The current findings are consistent with the modified glass dissolution model (Zavarin et al., 2004) which suggests that only  $\sim 4\%$  of the glass would dissolve in 100 days.

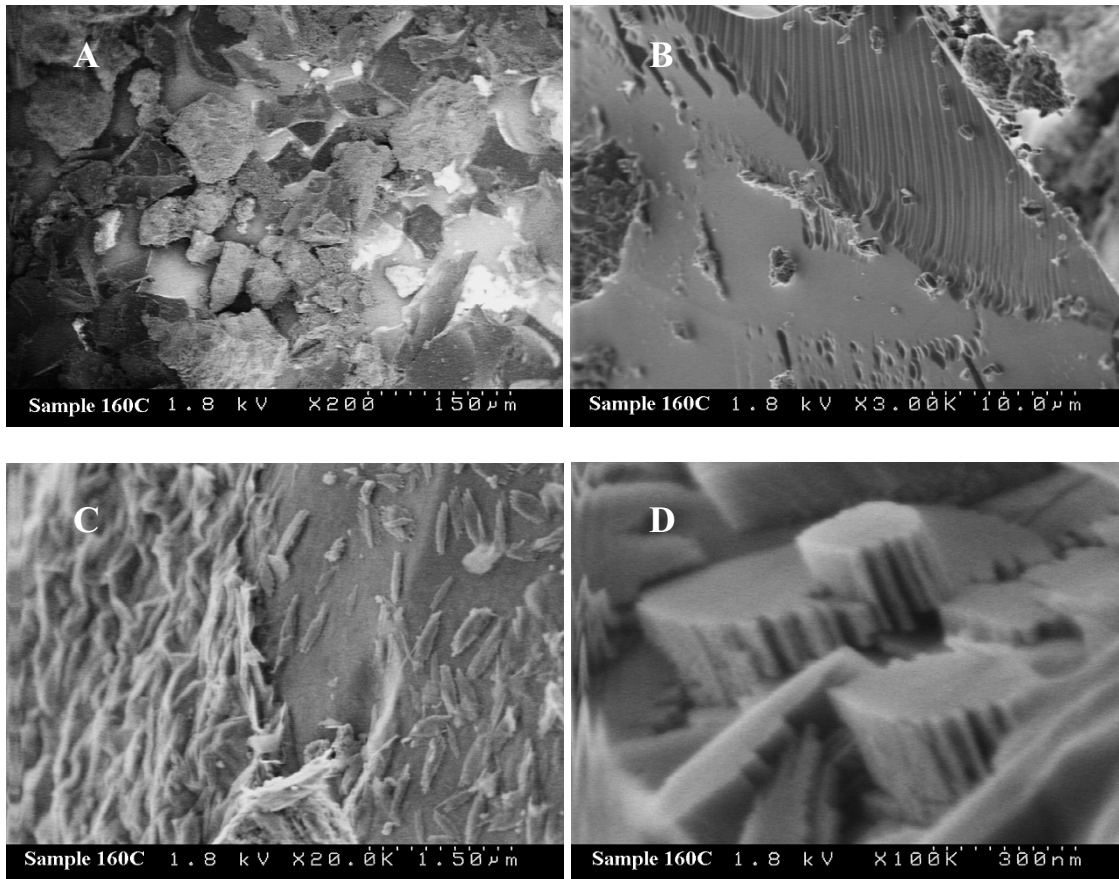


**Figure 10. SEM photomicrographs of nuclear melt glass reacted at 160°C.**

At 200°C, the appearance of the glass particles at a coarse scale does not seem to have changed significantly from the lower temperature samples (Figure 11A). However, the large degree of dissolution becomes quite evident at higher magnification. Again, even at this high temperature, it appears that some glass surfaces are more resistant to dissolution than others; certain surfaces show no evidence of glass dissolution (Figure 11A).

On certain glass surfaces, secondary minerals form as mats thick enough to obscure the underlying glass (Figures 11C, D, and E). The mats are composed of fibrous  $0.3 \times 1.5 \mu\text{m}$  secondary precipitates whose elemental composition appears similar to the underlying glass. In some cases, these fibrous secondary minerals appear to form in parallel alongside the intact glass (Figure 11F). At higher magnification, layers on the order of  $0.03 \mu\text{m}$  are observable within each of the fibrous secondary mineral particles (Figure 11G). A second mineral morphology, with rectangular blocky structure  $1 \times 2 \times 0.1 \mu\text{m}$ , is also observed (Figures 11H and 11I). This mineral morphology predominates along the leading edge of the strongly dissolving sides of glass particles.<sup>10</sup> These strongly dissolving glass surfaces have parallel dissolution lines (Figure 11J) also observed at lower temperatures to a much lesser degree (Figures 9B and 10B).

Based on the photomicrographs, we estimate that 1 to  $3 \mu\text{m}$  of the glass particle surfaces had dissolved and formed secondary precipitates in the 200°C experiment over ~3 months. If we assume a 1 to  $3 \mu\text{m}$  secondary mineral coating on  $50 \mu\text{m}$  particles, we can estimate that 6 to 17% of the glass had dissolved and formed secondary minerals. Since some of the glass appears to be unreacted, the fraction of glass dissolved is most likely at the low end of this estimate. The CHESHIRE model prediction (all glass dissolved in several days, Figure 6) does not compare favorably with this result. However, the modified glass model, which predicts ~50% glass dissolution over 100 days, is in much better agreement with this result.

The glass dissolution rates predicted by the modified glass model appear to be somewhat higher than observed in the 200°C experiment. However, the modified glass model was intended to be somewhat conservative (see Zavarin et al., 2004), particularly at high temperatures. Alternatively, as stated earlier, some aqueous Si in solution at 200°C may have precipitated out during sample cooling and prior to solution analysis. As a result, the saturation state ( $Q/K$ ) used in our model may be too low and the resulting predicted glass dissolution rate too fast. Thus, given the uncertainties of our model and the limitations of the data, the agreement between the modified glass dissolution model and observed dissolution/secondary mineral precipitation rates is quite good.

---

<sup>10</sup> It must be noted that what appears to be two distinct morphologies may not necessarily indicate two different secondary mineralogies.

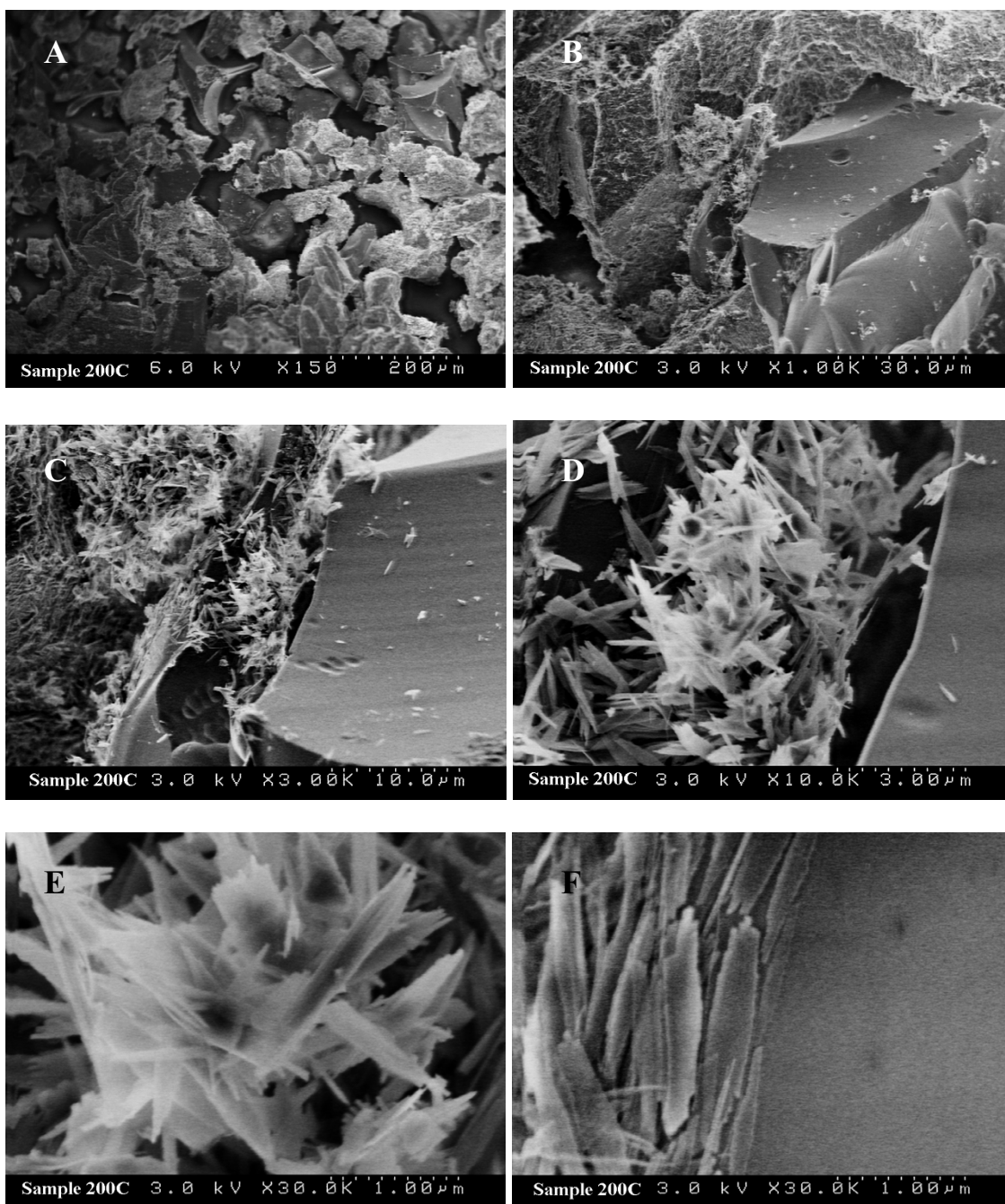


**Figure 11. SEM photomicrographs of nuclear melt glass reacted at 200°C.**

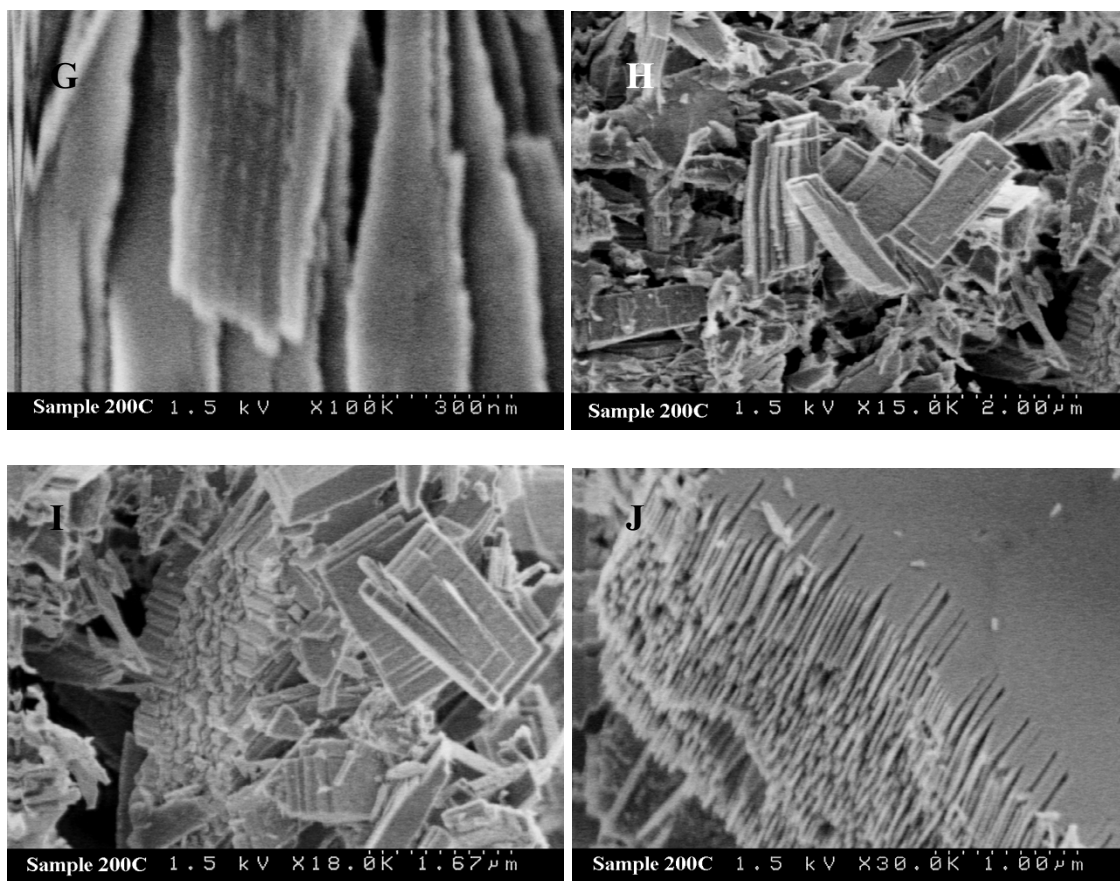
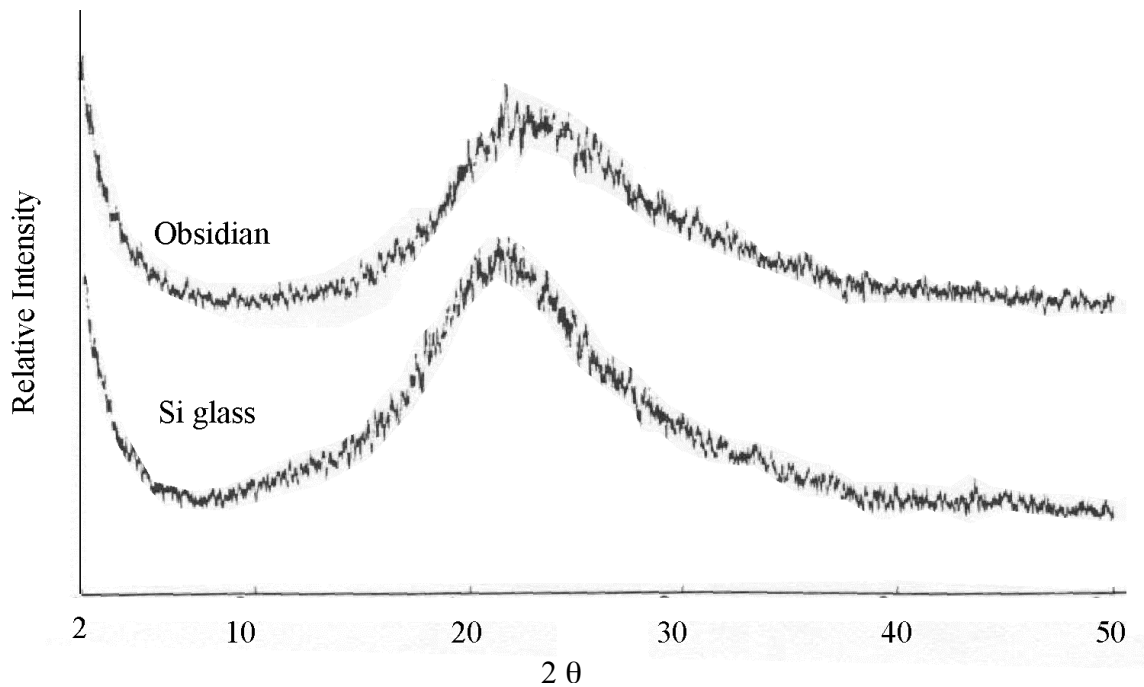


Figure 11 (continued). SEM photomicrographs of nuclear melt glass reacted at 200°C.

### 3.3.2 X-Ray Diffraction

XRD analysis was performed on reacted and unreacted samples. For reference, we show standard Si glass and obsidian glass XRD spectra in Figure 12 (from Palmer et al., 1988). Due to the amorphous nature of glass, XRD patterns of glasses typically contain a single broad peak over the range of 15 to 30 degrees  $2\theta$ . When compared to the XRD pattern of the unreacted nuclear melt glass (Figure 13), it appears that significant quantities of crystalline materials are present in the unreacted nuclear melt glass. This is evident by the many sharp peaks in the XRD pattern that are superimposed on the broad peak that can be attributed to the glass. These sharp peaks are not characteristic of a pure glass. From peak fitting, the unreacted nuclear melt glass was found to contain significant quantities of clinoptilolite with some possible mordenite, cristobalite, and quartz (aluminum peaks are related to the aluminum sample holder used during data collection) (Figure 14).

Unfortunately, it appears that there is sufficient clinoptilolite in the unreacted melt glass to obscure any subtle changes in sample mineral composition resulting from glass dissolution and secondary mineral precipitation. The lack of appearance of any new reflections in the XRD spectrum of the 200°C sample suggests either that the dominant secondary mineral precipitates in the reacted glasses are similar to those found in the unreacted glass or that insufficient quantities of secondary minerals were formed for observation by XRD. For all but the 200°C sample, it appears, from SEM, that the latter is likely. Due to the relatively large amount of secondary mineral formation at 200°C, the former may be the case for the 200°C experiment. Nevertheless, the identity of secondary minerals formed at the various temperatures cannot be determined without additional experiments. These experiments would include separation of secondary minerals from the primary glass and additional XRD analyses. The XRD data presented here only confirm that very small fractions of the glass dissolved at the temperatures investigated, consistent with the conservative modified glass dissolution model of Zavarin et al. (2004).



**Figure 12. XRD spectra of obsidian and laboratory-grade silica glasses. From Palmer et al. (1988). A stacked plot of relative intensities is presented.**

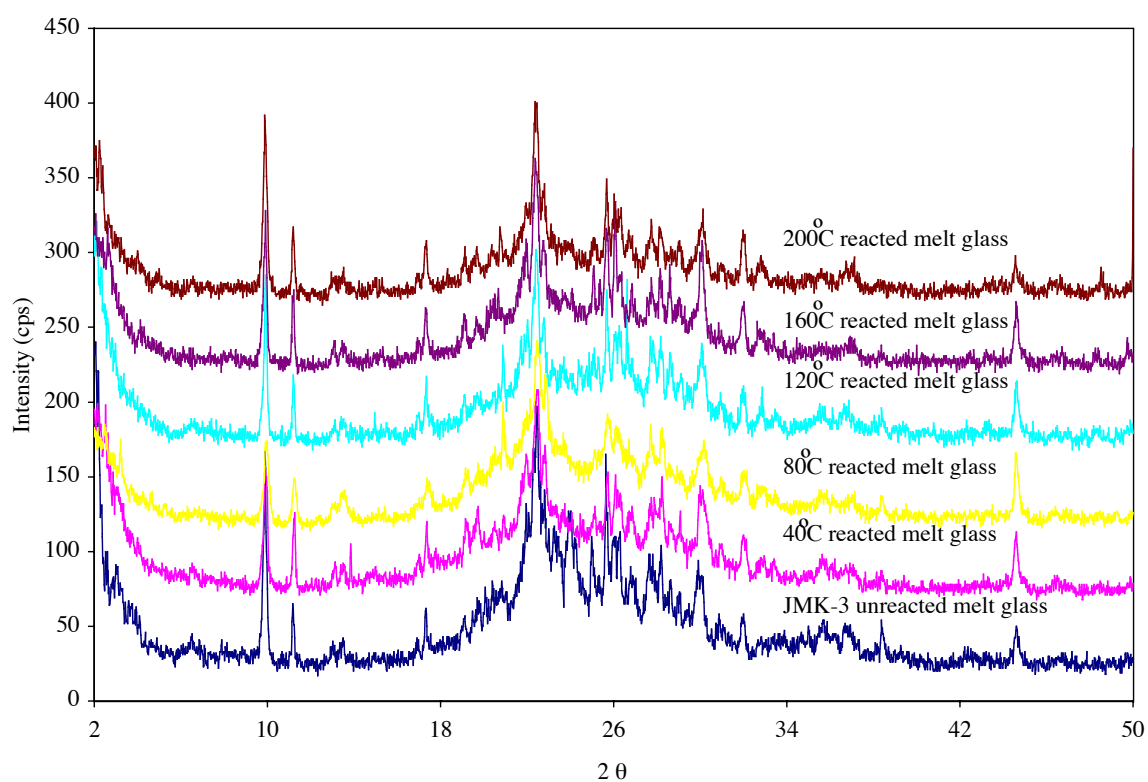


**Figure 13. XRD spectra of unreacted (JMK-3) and 40, 80, 120, 160, and 200°C reacted nuclear melt glasses. A stacked plot of relative intensities is presented.**



**Figure 14. Analysis of XRD data of unreacted and 200°C reacted nuclear melt glasses. Spectra were smoothed and background subtracted prior to peak fitting analysis.**



## 4 SUMMARY

We have reported on results from five nuclear melt glass dissolution/secondary mineral precipitation experiments conducted over a range of temperatures from 40 to 200°C. From the analysis of the fluids in contact with the melt glass and examination of the reacted melt glass itself, we find that:

- The pH of solutions tends to decrease with increasing temperature and exposure to dissolving melt glass. However, very large changes in pH are not observed. Interestingly, the alkalinity increases above 40°C, as evidenced by the higher pOH.
- Si concentrations in solution at the end of each experiment were always below that of a SiO<sub>2</sub>(am) saturated solution. For all but the 200°C experiment, solutions were supersaturated with respect to  $\alpha$ -cristobalite and undersaturated with respect to  $\beta$ -cristobalite. However, measured Si concentrations may underestimate true concentrations because of precipitation during sample cooling (and before sample analysis).
- Based on simulation of solution saturation states with respect to a variety of minerals, solutions were supersaturated with respect to K-feldspar in all but the 200°C solution; all solutions were close to saturation with respect to calcite, solutions were close to saturation with respect to beidellite and montmorillonite but greatly supersaturated with respect to nontronite and saponite end-member smectites; clinoptilolite appeared to be the most stable zeolite (though all but 200°C solutions were supersaturated with respect to this mineral); at 200°C, the relative stability of analcime and mordenite compared to clinoptilolite increased significantly.
- The Eh of solutions appears to decrease in high temperature experiments (160°C and 200°C). The reduced Eh will favor Pu in the +4 state as it is released from the melt glass. This has significant implications to Pu transport in the near field.
- The modified glass dissolution model reported in Zavarin et al. (2004) appears to predict the behavior of glass dissolution and secondary mineral precipitation rates more accurately than the CHESHIRE model of Pawloski et al. (2001).
- SEM photomicrographs show that glass dissolution and secondary mineral precipitation is not significant over a ~3 month time interval except at temperatures greater than or equal to 120°C.
- SEM photomicrographs show that glass dissolution appears to be very heterogeneous with some surfaces being resistant to dissolution while others show complex dissolution patterns.
- SEM photomicrographs show that the morphology of secondary minerals appears to be either fibrous 0.3×1.5  $\mu\text{m}$  rods or rectangular 1×2×0.1  $\mu\text{m}$  blocks. The latter morphology was only observed at 200°C. Both have a chemical composition similar to that of the underlying glass.
- XRD analysis did not provide evidence of significant secondary mineral formation partly because secondary minerals were already present in the

unreacted nuclear melt glass. The unreacted nuclear melt glass contained significant quantities of clinoptilolite with possibly some mordenite, cristobalite, and/or quartz. Since additional XRD peaks did not appear in the XRD spectrum of the 200°C reacted glass, it appears that secondary minerals are not unlike those observed in the unreacted glass. At lower temperatures, too little secondary minerals precipitated to expect significant changes in the bulk XRD patterns. Additional XRD analysis would be required to accurately identify secondary minerals.

## 5 ACKNOWLEDGEMENTS

Funding for this investigation was provided by the Environment Restoration Division's Underground Test Area Project at the U.S. Department of Energy, National Nuclear Security Administration, Nevada Site Office. This work was performed under the auspices of the U.S. Department of Energy by Lawrence Livermore National Laboratory under contract number W-7405-Eng-48.

## 6 REFERENCES

- Allen, P.G., Harris, L.J., Hudson, B., Laue, C.A., Loewen, D.R., Moran, J.E., Nelson, E.J., Pawloski, G.A., Rose, T.P., Ryerson, F.J., Smith, D.K., and Williams, R.W. (2003) Hydrologic Resources Management Program and Underground Test Area Project FY2001-2002 Progress Report, Rose, T.P., Eaton, G.A., and Kersting, A.B., Eds., UCRL-ID-154357, Lawrence Livermore National Laboratory, Livermore, California.
- Bourcier W. L., Carroll S. A., and Phillips B. L. (1994) Constraints on the affinity term for modeling long-term glass dissolution rates. *Mat. Res. Soc. Symp. Proc.* **333**, 507-512.
- Brunauer S., Emmett P. H., and Teller E. (1938) Adsorption of gases in multimolecular layers. *J. American Chemical Society* **60**, 309-319.
- Chipera, S.J., Bish, D.L., and Carlos, B.A. (1995) Equilibrium modeling of the formation of zeolites in fractures at Yucca Mountain, Nevada, In Natural Zeolites '93: Occurrence, Properties, Use (Ming, D.W. and Mumpton, F.A., eds.), International Committee on Natural Zeolites, New York.
- Grambow, B. (1987) Nuclear Waste Glass Dissolution: Mechanism, Model and Application, JSS Project, 87-02, SKB, Stockholm, October, 1987.
- Holler, H., and Worsching, U. (1978) Experiments on the formation of zeolites by hydrothermal alteration of volcanic glasses, In Natural Zeolites: Occurrence, Properties, Use (Sand, L.B. and Mumpton, F.A., eds.), Pergamon Press, New York.
- Johnson J. W. and Lundeen S. R. (1997) GEMBOCHS thermodynamic datafiles for use with the EQ3/6 modeling package. Lawrence Livermore National Laboratory, Livermore.

- Knauss K. G. and Peifer D. W. (1986) Reaction of Vitric Topopah Spring Tuff and J-13 Ground Water under Hydrothermal Conditions Using Dickson-Type, Gold-Bag Rocking Autoclaves. UCRL-53795, Lawrence Livermore National Laboratory, Livermore, California.
- Palmer, H.C., Tazaki, K., Fyfe, W.S., and Zhou, Z. (1988) Precambrian glass. *Geology*, 16:221-224.
- Papelis, C., Um, W., Russell, C.E., and Chapman, J.B. (2000) Measuring the specific surface area of natural and man-made glasses. Effect of formation process, morphology, and particle size. *In* Determination of Reactive Surface Area of Melt Glass, Bourcier, W. Roberts, S., Smith, D.K., Hulsey, S., Newton, L., Sawverl, A., Bruton, C., Papelis, C., Um, W., Russel, C.E., and Chapman, J., UCRL-ID-145181, Lawrence Livermore National Laboratory, Livermore, California.
- Pawloski G. A., Tompson A. F. B., and Carle S. F. (2001) Evaluation of the Hydrologic Source Term from Underground Nuclear Tests on Pahute Mesa at the Nevada Test Site: The CHESHIRE Test, Bourcier, W.L., Bruton, C.J., Carle, S.F., Daniels, J.I., Maxwell, R.M., Pawloski, G.A., Shumaker, D.S., Smith, D.K., Tompson, A.F.B., and Zavarin, M., Contributors. UCRL-ID-147023, Lawrence Livermore National Laboratory, Livermore, California.
- Warren R. G., Sawyer D. A., Byers F. M., Jr., and Cole G. L. (2000) A Petrographic/Geochemical Database and Stratigraphic Framework for the Southwestern Nevada Volcanic Field, Vol. 2000. National Oceanic and Atmospheric Administration.
- Zavarin M., Roberts S.K., Zhao P., Williams R.W., Rose T.P., Rainier A., and Pawloski G. A. (2004) High-Temperature Studies of Glass Dissolution Rates Close to Saturation. UCRL-TR-204874, Lawrence Livermore National Laboratory, Livermore, California.

**APPENDIX. SEM PHOTOMICROGRAPHS OF UNREACTED NUCLEAR MELT GLASS (SAMPLE JMK-3) AND REACTED MELT GLASS (80°C, 120°C, 160°C AND 200°C).**

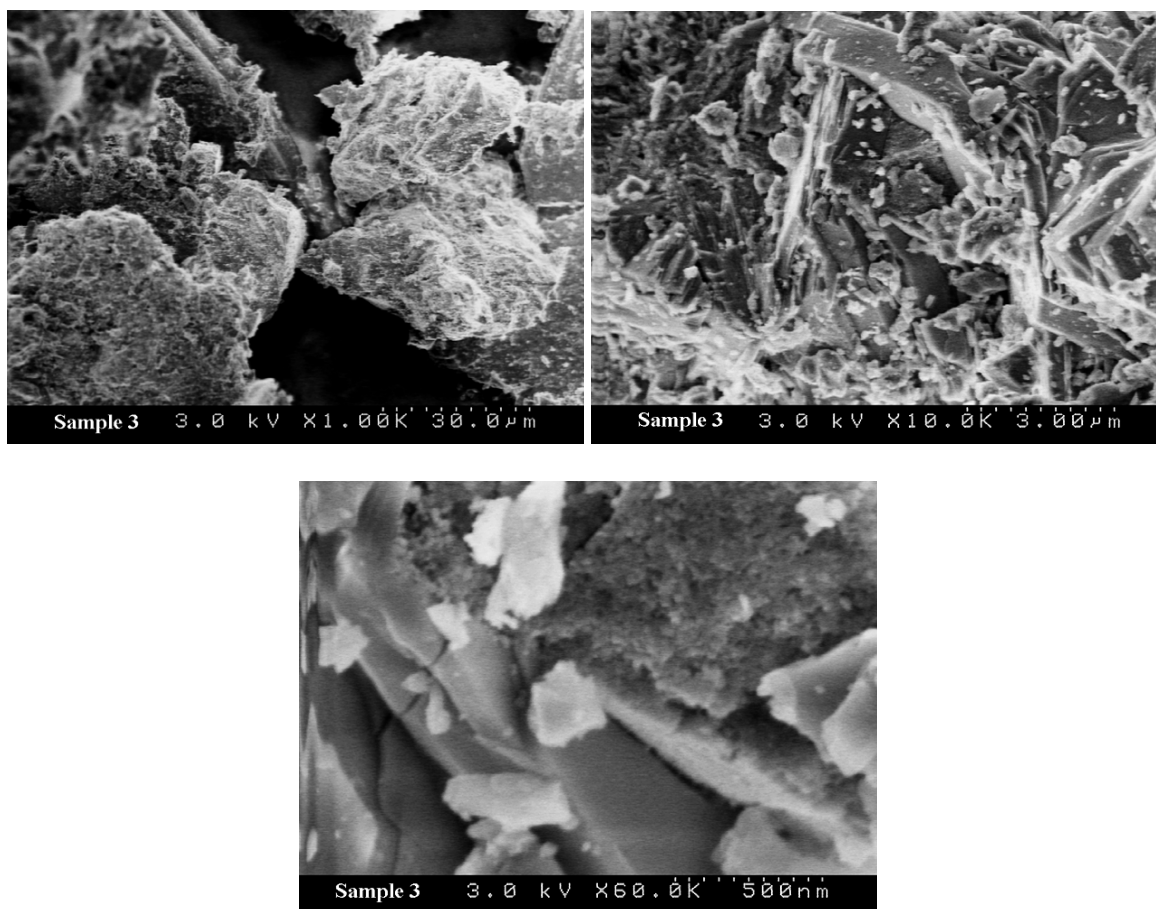


**Figure A1. SEM results for the unreacted nuclear melt glass (sample JMK-3).**

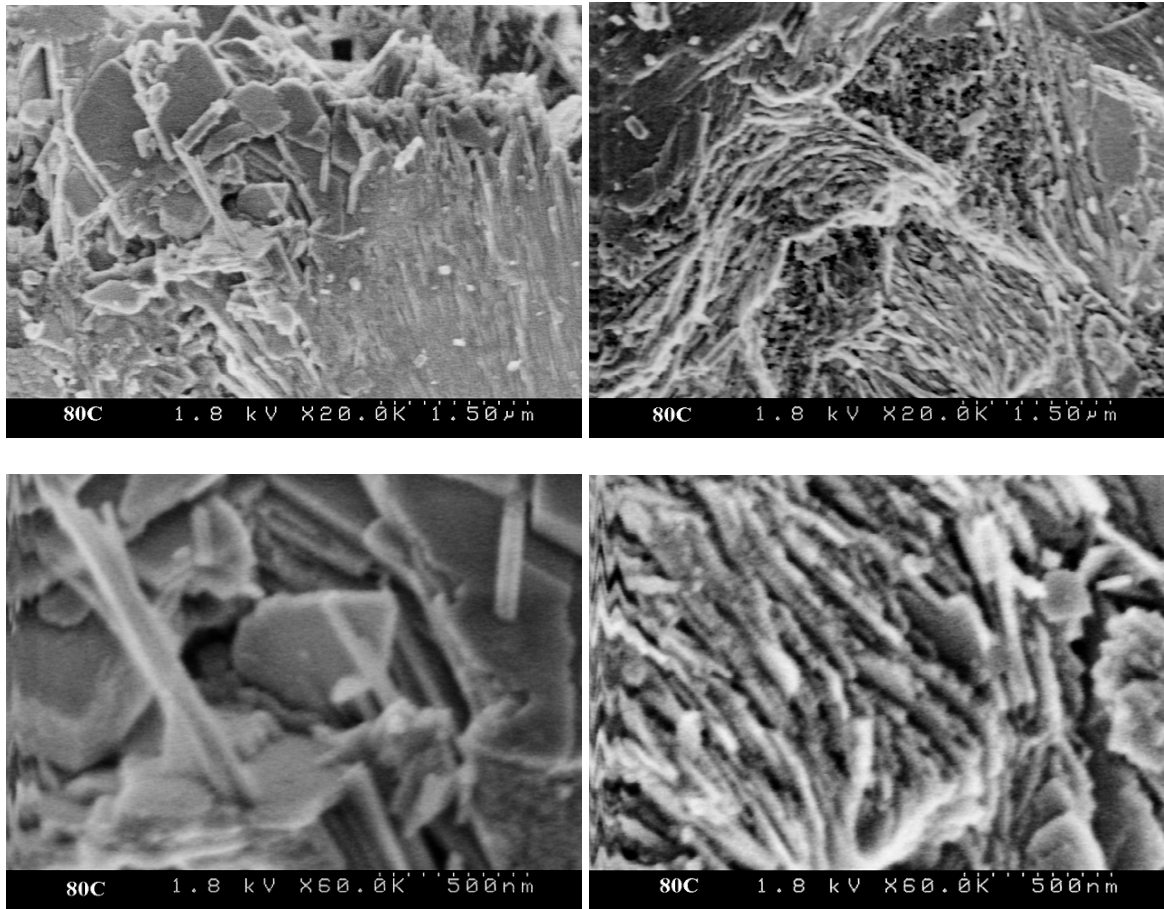


**Figure A2. SEM results for the 80°C reacted nuclear melt glass.**

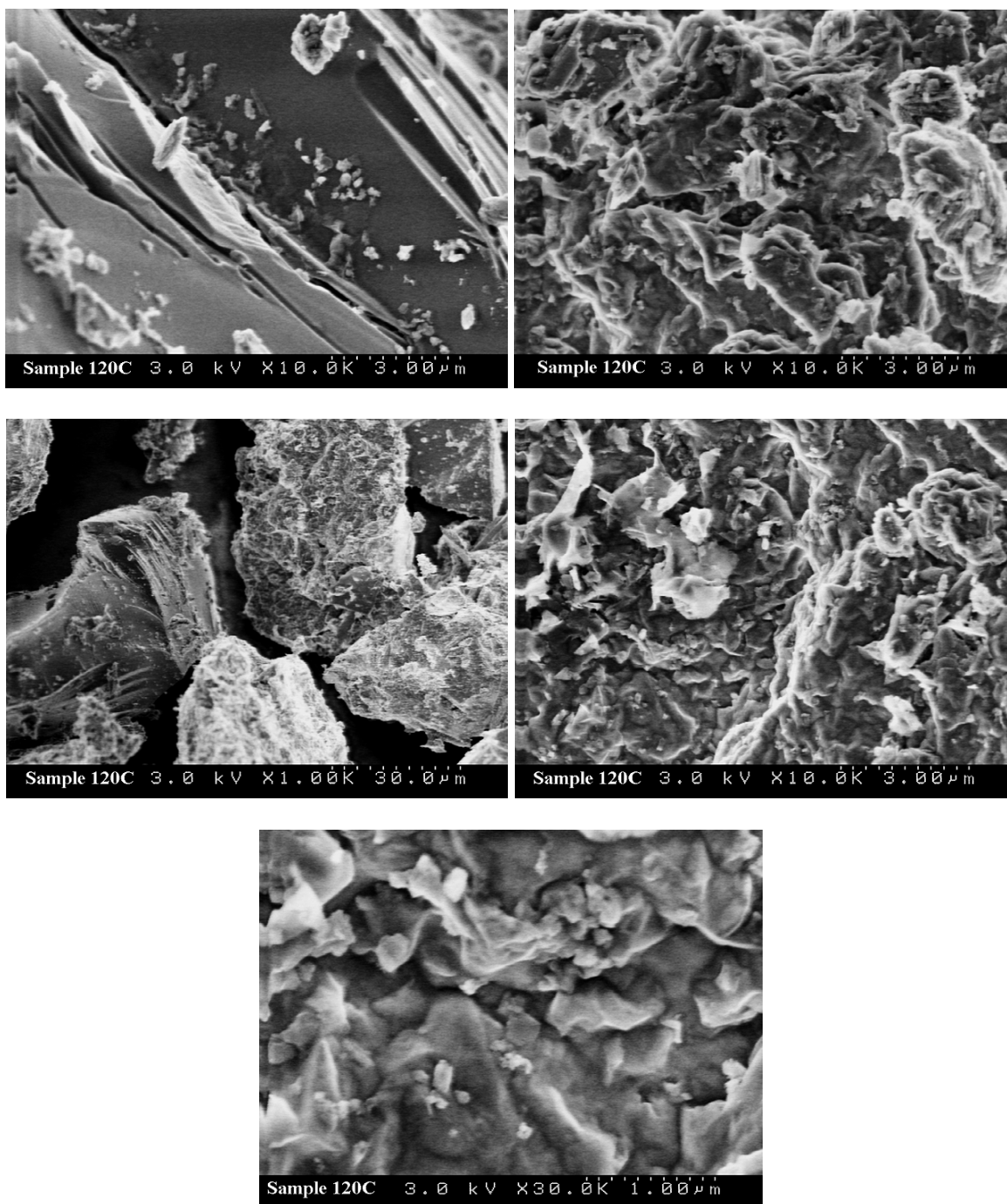


**Figure A3. SEM results for the 120°C reacted nuclear melt glass.**

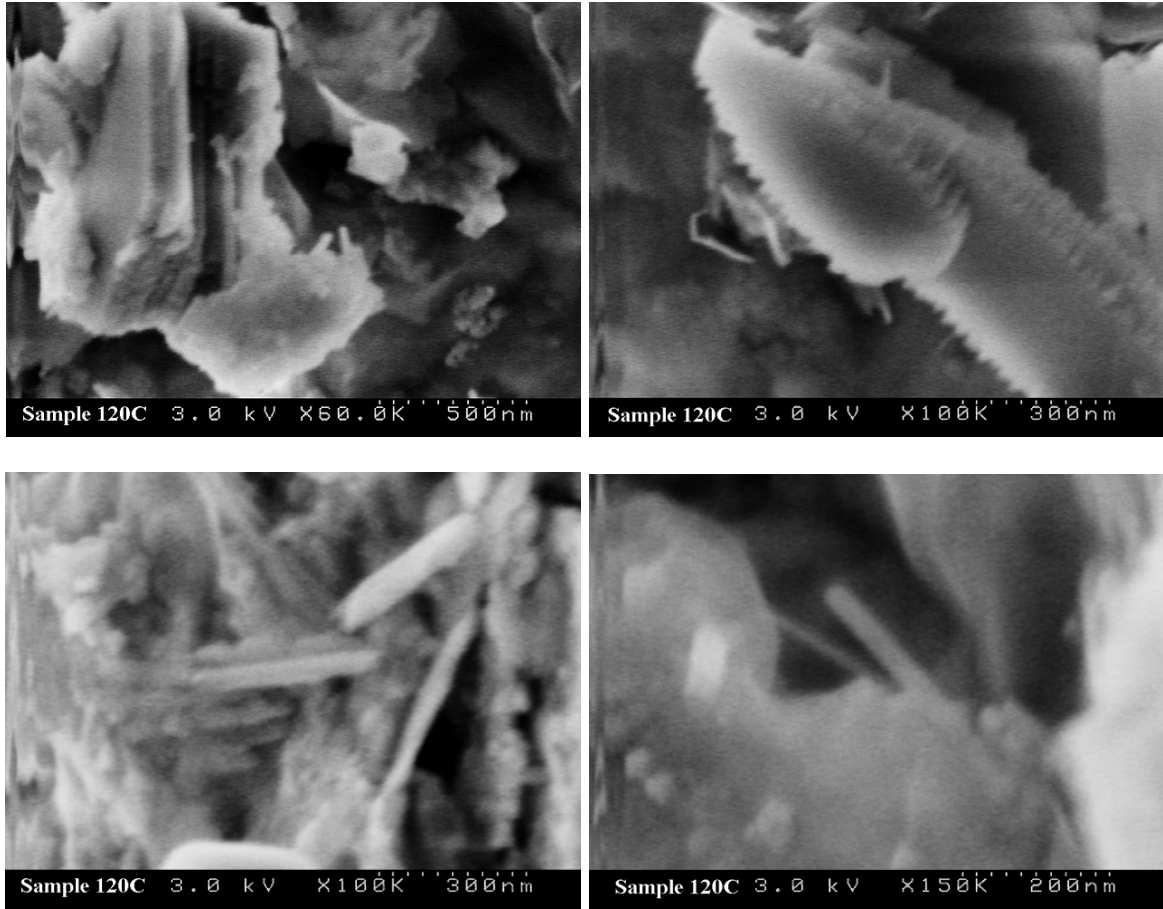
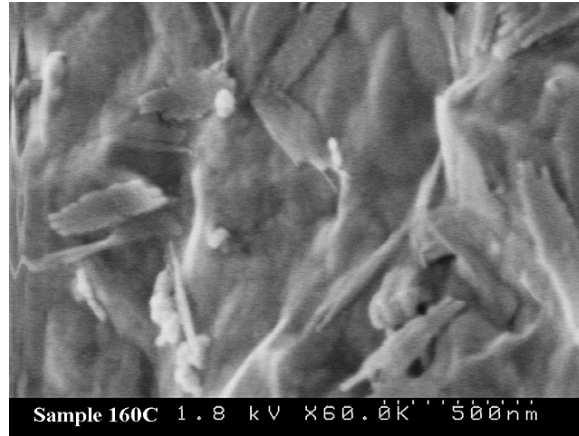
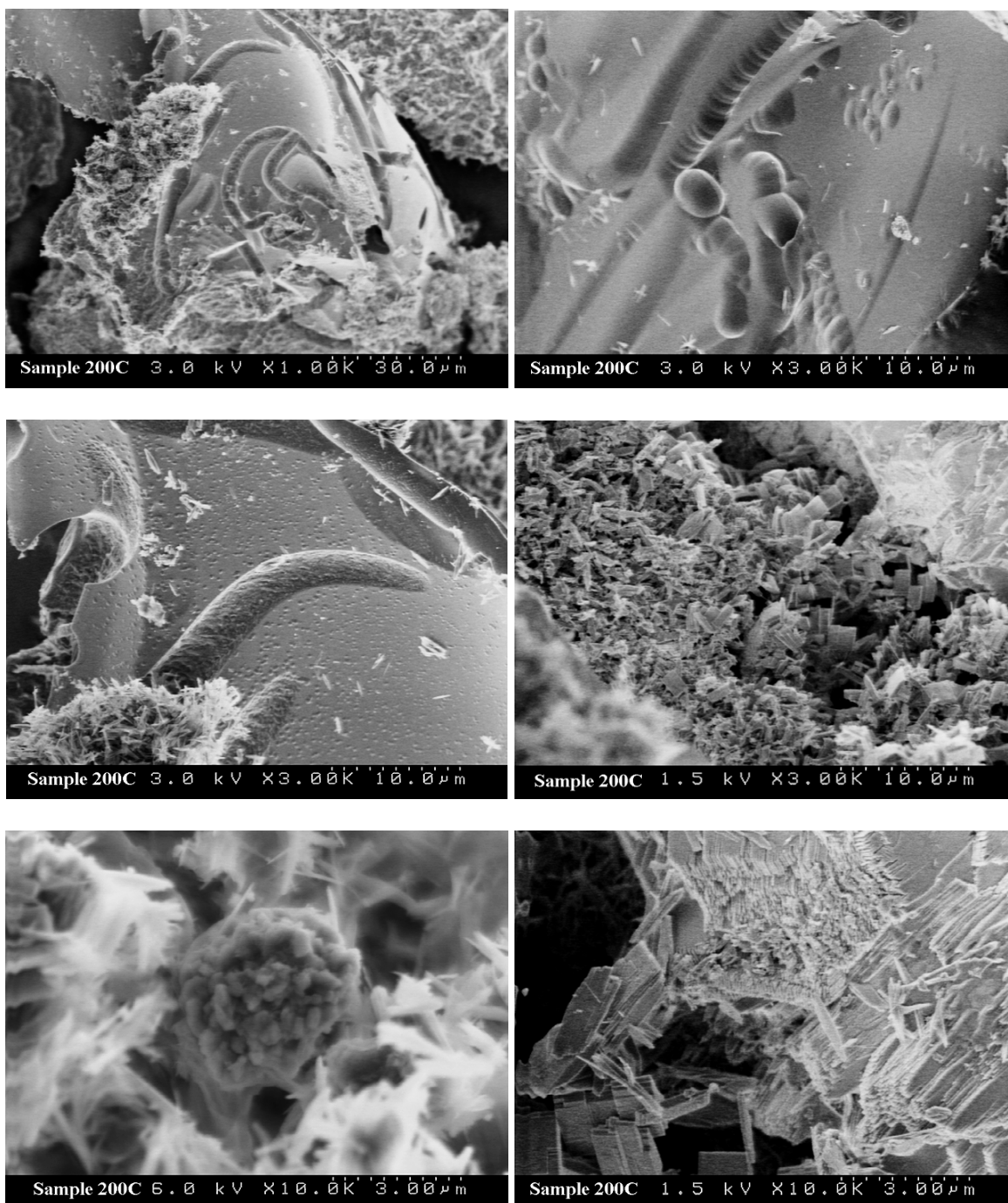


Figure A3 (continued). SEM results for the 120°C reacted nuclear melt glass.



**Figure A4. SEM results for the 160°C reacted nuclear melt glass.**





**Figure A5. SEM results for the 200°C reacted nuclear melt glass.**

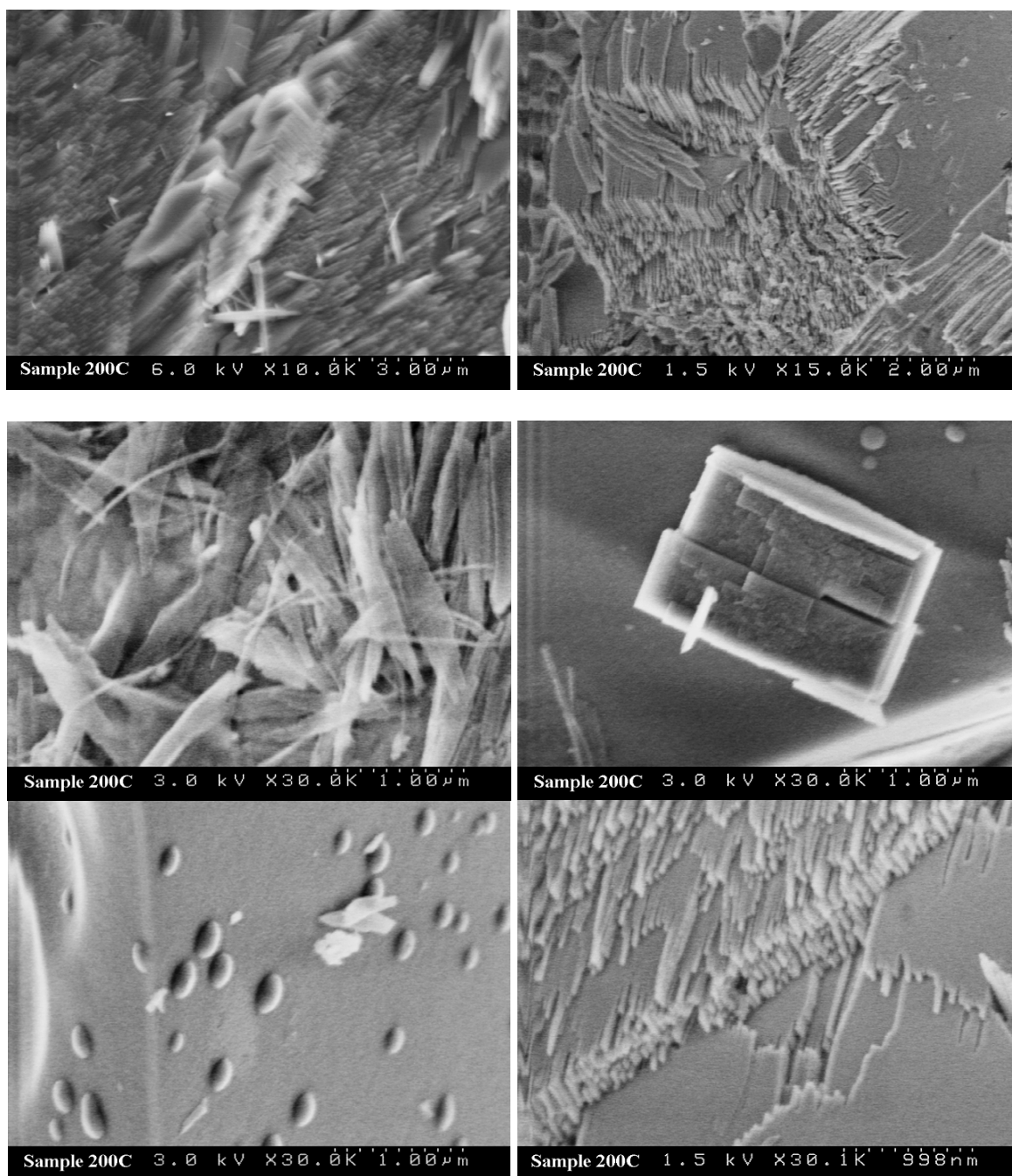


Figure A5 (continued). SEM results for the 200°C reacted nuclear melt glass.